

Hydroacoustic Travel Time Variations as a Proxy for Passive Deep-Ocean Thermometry A Cookbook

Smets, P.S.M.; Weemstra, C.; Evers, L.G.

DOI

[10.1029/2022JC018451](https://doi.org/10.1029/2022JC018451)

Publication date

2022

Document Version

Final published version

Published in

Journal of Geophysical Research: Oceans

Citation (APA)

Smets, P. S. M., Weemstra, C., & Evers, L. G. (2022). Hydroacoustic Travel Time Variations as a Proxy for Passive Deep-Ocean Thermometry: A Cookbook. *Journal of Geophysical Research: Oceans*, 127(5), Article e2022JC018451. <https://doi.org/10.1029/2022JC018451>

Important note

To cite this publication, please use the final published version (if applicable).
Please check the document version above.

Copyright

Other than for strictly personal use, it is not permitted to download, forward or distribute the text or part of it, without the consent of the author(s) and/or copyright holder(s), unless the work is under an open content license such as Creative Commons.

Takedown policy

Please contact us and provide details if you believe this document breaches copyrights.
We will remove access to the work immediately and investigate your claim.

Hydroacoustic Travel Time Variations as a Proxy for Passive Deep-Ocean Thermometry—A Cookbook



Key Points:

- Travel time variations extracted from time-lapse cross-correlations between a hydrophone station and a three-component broadband seismometer
- Frequency-dependent acoustic travel time serves as path-averaged temperature changes in the Sound Fixing and Ranging channel
- Selecting eligible cross-correlations by source activity and slowness estimation is crucial for extracting reliable oceanic travel times

Supporting Information:

Supporting Information may be found in the online version of this article.

Correspondence to:

P. S. M. Smets,
mail@pietersmets.be

Citation:

Smets, P. S. M., Weemstra, C., & Evers, L. G. (2022). Hydroacoustic travel time variations as a proxy for passive deep-ocean thermometry—A cookbook. *Journal of Geophysical Research: Oceans*, 127, e2022JC018451. <https://doi.org/10.1029/2022JC018451>

Received 17 JAN 2022
 Accepted 2 MAY 2022

Author Contributions:

Conceptualization: P. S. M. Smets, C. Weemstra
Data curation: P. S. M. Smets
Formal analysis: P. S. M. Smets, C. Weemstra
Funding acquisition: L. G. Evers
Investigation: P. S. M. Smets
Methodology: P. S. M. Smets, C. Weemstra
Project Administration: L. G. Evers
Resources: P. S. M. Smets
Software: P. S. M. Smets
Supervision: C. Weemstra, L. G. Evers
Validation: P. S. M. Smets
Visualization: P. S. M. Smets

© 2022. The Authors.

This is an open access article under the terms of the [Creative Commons Attribution License](https://creativecommons.org/licenses/by/4.0/), which permits use, distribution and reproduction in any medium, provided the original work is properly cited.

P. S. M. Smets^{1,2} , C. Weemstra^{1,2} , and L. G. Evers^{1,2} 

¹Department of Geoscience and Engineering, Delft University of Technology, Delft, The Netherlands, ²R&D Seismology and Acoustics, Royal Netherlands Meteorological Institute, De Bilt, The Netherlands

Abstract We report on the extraction of deep ocean travel time variations from time-lapse cross-correlations between a hydrophone station and a three-component broadband seismometer. The signals we cross-correlate in this study result from repeated activity by the Monowai seamount, one of the most active submarine volcanoes of the Tonga-Kermadec ridge. In particular, we introduce a specific workflow to exploit repetitive hydroacoustic underwater source activity, which we detail to such an extent that it serves as an example (or “cookbook”). For this reason, we have made the source code publicly available. The workflow proposed in this study (a) overcomes differences in instrument sensitivity and sample rates, (b) involves the selection of eligible cross-correlations based on a source activity criterium as well as slowness analysis, and (c) extracts the travel time variations in distinct frequency bands. In our case, the two frequency bands are 3–6 and 6–12 Hz. We find that the estimated travel time variations in both frequency bands consist of a complex periodic pattern superimposed on a robust linear trend. This linear trend is decreasing, which we attribute to increasing water temperatures along the propagation path of the hydroacoustic signals.

Plain Language Summary We extract variations in the ocean travel time between submerged microphones and a seismometer on an island. The signals in this study result from repeated activity by the Monowai seamount, one of the most active submarine volcanoes of the Tonga-Kermadec ridge. The travel time variations result from a time-lapse similarity analysis. In particular, we introduce a specific workflow to exploit repetitive underwater source activity. We detail it to such an extent that it serves as an example (or “cookbook”). For this reason, we have made the source code publicly available. The workflow proposed in this study (a) overcomes discrepancies in instrument sensitivity and sampling rates, (b) involves the selection of qualified signals based on a source activity criterium as well as directional analysis, and (c) extracts the travel time variations in distinct frequency bands. The estimated travel time variations consist of a complex periodic pattern superimposed on a robust linear trend. Moreover, this linear trend is decreasing, which we attribute to increasing water temperatures along the propagation path of the hydroacoustic signals.

1. Introduction

For a few years, the interest in passive deep-ocean thermometry utilizing hydrophone stations of the International Monitoring System (IMS) has increased considerably. These permanent stations are established as a verification measure for the Comprehensive Nuclear-Test-Ban Treaty (CTBT; Dahlman et al., 2009b). Eleven stations constantly monitor the oceans for hydroacoustic evidence of a potential nuclear test (Dahlman et al., 2009a). Six underwater hydrophone stations, consisting of one or two hydrophone triplets, form the backbone of the hydroacoustic network. Five land-based seismometers, positioned upon steep-sloped islands to measure the acoustic-to-seismic coupled energy or T-phase, provide additional coverage. The hydrophones are suspended in the SOund Fixing and Ranging (SOFAR) channel. The SOFAR channel is a low-velocity layer in the ocean that acts as an acoustic waveguide, facilitating sound to travel nearly horizontally for thousands of kilometres (Woolfe et al., 2015). As sound travels through the SOFAR channel, the loss of sound energy through interaction with the sea surface and the ocean floor is minimized, making it possible to propagate efficiently for thousands of kilometres. The frequency bandwidth of interest for this work ranges between 1 and 40 Hz. The ambient hydroacoustic wavefield is mainly due to earthquakes (de Groot-Hedlin, 2005; Evers & Snellen, 2015), underwater volcanoes (Green et al., 2013; Metz et al., 2016; Watts et al., 2012), marine mammals (Prior et al., 2012), and icebergs (Evers et al., 2013; Matsumoto et al., 2014; Talandier et al., 2006). Since 2020, the Marine Strategy Framework Directive (MSFD, 2008) requires EU Member States to ensure good environmental Status of EU marine waters. Passive techniques utilizing the ambient wavefield are encouraged above potentially harmful

Writing – original draft: P. S. M. Smets
Writing – review & editing: P. S. M. Smets, C. Weemstra, L. G. Evers

active anthropogenic sources to probe the ocean and the solid layers beneath. Lately, Kuna and Nábělek (2021) have successfully mapped out the density of the ocean crust, a vital part of exploring the seafloor, using fin whale vocalizations as a natural source.

Several studies have shown the potential of hydroacoustic thermometry in the SOFAR channel by stationary-phase estimations of ridge earthquakes (Evers & Snellen, 2015) and by cross-correlating ambient signals recorded at two different IMS stations (Evers et al., 2017; Woolfe et al., 2015). Both passive thermometry methods intend to extract phase velocities from retrieved Green's functions, yielding valuable information regarding the constitutive parameters and density of the medium. However, in a seismic interferometric context, time-averaged cross-correlations may result in the Green's function between a pair of receivers given a fully equipartitioned wavefield (Roux & Kuperman, 2004; Wapenaar et al., 2005; Weaver & Lobkis, 2001). For an anisotropic wavefield, sources located near the line of sight between the two receivers, the so-called Fresnel zones, suffice to approximate the true Green's function (Snieder, 2004; Wapenaar et al., 2010). Considering the IMS hydrophone stations, bathymetric blocking typically limits the relevant sources to the single-sided Fresnel zone, for example, iceberg noise from the Antarctic Circumpolar (Evers et al., 2017; Sambell et al., 2019; Woolfe & Sabra, 2015). Accordingly, only the single-sided Green's function can be retrieved, that is, without its time reversal. In addition, the considered hydroacoustic wavefield is non-isotropic. For example, Arctic sources have distinct propagation characteristics compared to equatorial sources. Furthermore, bathymetric blocking limits the sets of distinct interstation couples to only two. A direct sound path only exists between the triplets north and south of H10 and H11, at Ascension Island and Wake Island, respectively. The small aperture of an IMS hydrophone triplet prohibits the application to receiver couples within the triplet (Sambell et al., 2019). The short receiver spacing and the single-sided response are too sensitive to directional changes, resulting in significant errors in the estimated velocity and changes. An accurate estimation of a Green's function and the phase velocity between two IMS hydrophones is therefore challenging.

Recently, W. Wu et al. (2020) introduced a method to infer basin-scale deep-ocean temperature changes from sound waves generated by repeating ridge earthquakes. The travel time method does not use Green's functions to infer temperature changes. W. Wu et al. (2020) retrieved travel time variations from cross-correlation analysis of remote hydroacoustic signals. The acoustic signal samples the deep ocean along its path as a function of range and depth, represented by the sensitivity kernel, and yields an integrated response in terms of the travel time. Seismic *P* waves, observed by at least one seismic reference station near the epicenter, constrain the hydroacoustic signals to obtain relative travel times. The travel time variations are associated with path-averaged changes in the deep-ocean temperature, consistent with the deep-ocean warming indicated by Estimating the Circulation and Climate of the Ocean (<https://ecco-group.org>).

Inspired by the earlier work of Metz et al. (2016), in this study, distant hydroacoustic observations of the Monowai volcanic center (MVC) are cross-correlated with “closer” seismic T-phase observations. The MVC marks the midpoint of the ~2,500 km long Tonga-Kermadec ridge, located northeast of New Zealand (Davey, 1980). The hydroacoustic activity of the submarine volcanic center is repeatedly observed by distant IMS hydrophone stations, located near Juan Fernández Islands in the South Pacific Ocean and Ascension Island in the South Atlantic Ocean (Figure 1). T-phase converted energy recorded at a “close” broadband seismic station on Rarotonga (~1,850 km) is used as a reference to estimate the relative travel time of the sound to a distant hydrophone. In contrast to W. Wu et al. (2020), the cross-correlation directly yields the relative travel time not needing a specific seismic phase to constrain the signals. However, to overcome the variations in transfer functions and non-identical sampling rates of the different instruments, Metz et al. (2016) proposed to cross-correlate the normalized root-mean-square amplitude using one-minute windows to obtain the relative travel time. Seismic and hydroacoustic data were first band-pass filtered at 2–6 and 4–12 Hz, respectively. Notwithstanding retrieving the relative travel time, many spectral and all phase information was lost.

We extend the two-receiver method of Metz et al. (2016) to a two-location method composed of a triplet hydrophone station and a three-component broadband seismometer as the reference. The hydrophone triplet allows array processing techniques, for example, directional analysis, improving the overall robustness. Using all three seismometer components provides three orthogonal observations: the vertical, radial, and transverse components. In addition, it allows particle motion analysis which may provide additional information regarding acoustic-to-seismic coupling in the vicinity of the seismometer. We limit seismic waves to the vertical plane to estimate travel time variations (vertical and radial components only). A pre-processing workflow is proposed that retains

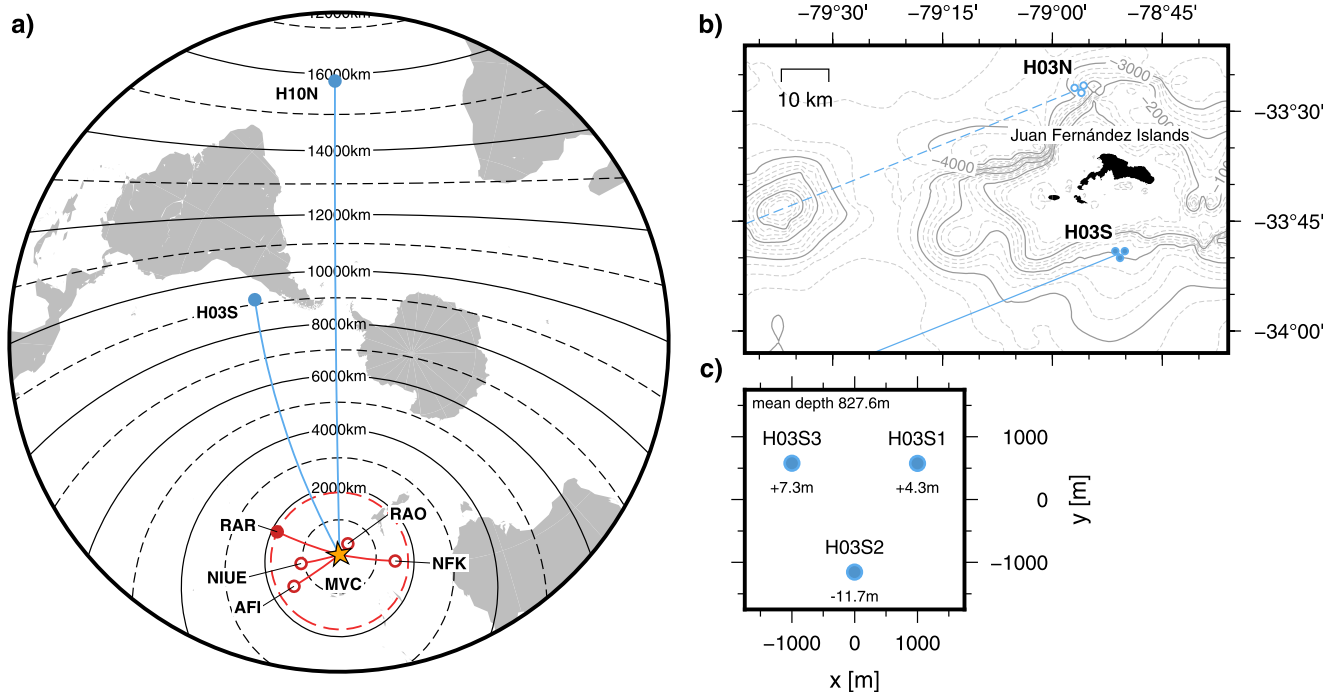


Figure 1. (a) Map of the Monowai volcanic center (MVC, yellow star), broadband seismic stations within a 2,000 km radius (red circles) and hydroacoustics triplets H03S and H10N (blue circles). Solid circles indicate a direct line of sight through the SOund Fixing and Ranging (SOFAR) channel. (b) Map depicting the hydrophone triplets H03N (obstructed line of sight) and H03S (direct line of sight) near the Juan Fernández Islands, Chile. (c) Hydrophone triplet layout in local coordinates; vertical deviation from mean depth is indicated for the individual elements.

phase and spectral information for the cross-correlation analysis. We minimally pre-process waveforms in the sense that cross-correlation functions (CCFs) can be filtered later in the workflow retaining as much spectral information as possible. We propose an automatic selection criterion to account for non-continuous and spurious MVC activity. We extract frequency-dependent travel time variations from time-lapse cross-correlations for the eligible periods.

This work intends to be a “cookbook” study based on FAIR data principles (Findable, Accessible, Interoperable, and Reusable; Wilkinson et al., 2016) and fostering reusability and reproducibility. For that reason, we discuss typically trivial parts in rather great detail. To limit the divergence of the analyses and discussions, however, only the hydrophone triplet H03S and the three-component seismometer at station RAR with location code 10 will be used. Notwithstanding, the presented two-location method is directly applicable to other instruments and repetitive stationary sources. The source code and examples are publicly available (<https://github.com/psmsmets/xcorr>).

The work is structured as follows. Hydrophone triplets and potential high-quality seismic stations are discussed in detail in Section 2. The pre-processing workflow is proposed in Section 3. Section 4 explains the linear unbiased digital cross-correlation applied in the frequency domain. The automatic selection criterion is given in Section 5 and the time-lapse analysis in Section 6. Section 7 discusses travel time variations as a proxy for changes in deep-ocean temperature. CCFs of the vertical and radial seismic components of RAR are analyzed in Section 8 to investigate the acoustic-to-seismic conversion. Discussions and conclusions follow in Section 9.

2. Instrumentation

Locations of the MVC and considered instruments for the two-location method are indicated in Figure 1a. We consider only high-quality instruments part of a permanent and autonomous station. Table 1 gives an overview of the instruments, sampling rates, and start times as well as the corresponding SEED-ID. The SEED data identification format uses four name components to uniquely identify a time series and provide attribution to the

Table 1
Considered Broadband Seismometers and Hydrophone Triplets Represented by Their SEED-ID

Net.	Sta.	Loc.	Channel	Sps	Instrument	Start time
AU	NIUE		BH[N,E,Z]	40	Streckeisen STS-2	2007–263
AU	NFK		BH[N,E,Z]	40	Streckeisen STS-2	2008–141
IU	AFI	10	BH[1,2,Z]	40	Streckeisen STS-2.5	2013–212
IU	RAR	10	BH[1,2,Z]	40	Streckeisen STS-2	2010–061
IU	RAO	00	BH[1,2,Z]	40	Streckeisen STS-2.5	2013–137
IM	H03S[1–3]		EDH	250	HiTech	2014–114
IM	H10N[1–3]		EDH	250	HiTech	2004–258

Note. The SEED-ID are the first four columns: network, station, location and channel code. Remaining columns are the sampling rate, the instrument brand and type, and the start year and the day of the year.

owner of the data: two-character network code, three-character station code, two-character location ID and a three-character channel code. Table 2 lists the locations and the related geodetic distance and bearing to the MVC for the used hydrophone stations and seismometer.

In order to be able to compute the time-lapse cross-correlations between two stations, both require a direct line of sight through the SOFAR channel. Hence, not all stations are suitable. Blocking is not limited to islands and landmasses but may also be due to bathymetric features protruding the SOFAR channel, for example, seamounts and ridges. A seafloor depth smaller than 500 m is used as a first-order approximation for potential blockage in shallow water. The latter approximates one acoustical wavelength at 3 Hz, corresponding to the lower cutoff frequency of the SOFAR channel (e.g., Jensen et al., 2011).

Furthermore, the cross-correlation analyses depend on high-quality data, including well-defined station and instrument metadata for the hydrophone and seismometer stations used in this study. Since several stations have non-negligible issues, some additional background information and motivation are given in the following two subsections explaining why we discard a station or which additional processing measures are needed.

2.1. Hydrophone Triplets

H03 and H10, at Juan Fernández Islands and Ascension Island, respectively, are each composed of two triplets located north and south of the islands. Table 1 lists the instrumentation and SEED-ID's. Each hydrophone triplet forms an equilateral triangle with an intersensor distance of approximately 2 km (Dahlman et al., 2009a). The hydrophones are suspended in the middle of the SOFAR channel by a submerged float and moored to a main cable on the sea floor by the so-called riser cable. The riser cable lengths depend on the local bathymetry such that the triplet floats near-horizontal in approximately the center of the SOFAR channel. The bottom-moored triplet is maintained stationary by the floats and riser cables; however, streaming of the water can cause minor variations in true location (Nichols & Bradley, 2017). The consistency in riser cable length is vital to preserve the relative shape of the array. The main cable is deployed from the shore into the ocean to provide power and communication to the three instruments. The hydrophones have a flat amplitude response within 1–100 Hz and sample at 250 Hz (Dahlman et al., 2009a).

Both northern and southern triplets at H03 and H10 do observe the hydroacoustic activity of the MVC. All four triplets, however, are not equally suitable. At Juan Fernández Islands, the northern triplet H03N is partly obstructed due to a seamount approximately 50 km to the West (see Figure 1b). The obstruction yields a significantly lower signal-to-noise ratio than southern triplet H03S. At Ascension Island, electronic noise significantly impacts the southern triplet H10S and, in particular, element H10S1. Detection of hydroacoustic activity is possible; however, the overall triplet sensitivity is affected. Furthermore, the studies of Evers et al. (2017) and Takagi et al. (2015) indicate the

Table 2
Selected Station Locations With Their Distance and Bearing to the MVC

Station	Lat (deg)	Lon (deg)	Elev (m)	Dist (km)	Bearing (deg)
RAR	−21.21250	−159.77330	28	1,850.1	250.39
H03S1	−78.90575	−33.84370	−752	9,158.5	243.92
H03S2	−78.92619	−33.83696	−745	9,157.1	243.93
H03S3	−78.90948	−33.82584	−754	9,159.0	243.92

presence of repetitive electronic noise of the H10 data loggers causing spurious coherent cross-correlations. The spurious cross-correlations correspond to high coefficients at zero lag time between 2005 and 2009. In summary, we only recommend the southern triplet H03S and the northern triplet H10N.

In this study, we consider only H03S. However, the methodology is directly applicable to any horizontal hydrophone array. Data availability of H03 starts in April 2014. No earlier data for this configuration and instrumentation are available since H03 was compromised in 2010 by a tsunami and reinstalled in 2014 (Haralabus et al., 2014). Riser cable lengths of the elements H03S[1–3] are 1,208, 1,344, and 1,176 m, respectively. H03S has a tilt of 0.6° with an angle of maximal plunge toward the South (171.6° clockwise from North). Tilting of the triplet, when assumed to be horizontal, can cause a deviation between the actual and resolved horizontal slowness (Edwards & Green, 2012). If the assumption is used that the hydrophones are all at the same depth in the water column, then the horizontal propagation velocity error is maximal along the slope direction ($171.6^\circ \pm 180^\circ$) whereas the back azimuth error is maximal normal to the slope ($261.6^\circ \pm 180^\circ$). Assuming a low inclined signal from the MVC direction (30° inclination and 243.92° back azimuth) and a local speed of sound of $1,481.7 \text{ m s}^{-1}$ (World Ocean Atlas 2013, Locarnini et al., 2013; Zweng et al., 2013), the resulting errors when ignoring the vertical-coordinate contributions are 3.09 m s^{-1} and 0.32° , for the horizontal propagation velocity and back azimuth, respectively. For near-horizontal signals, the errors are minor. The vertical extent of the triplet has a negligible contribution to the observed time delay for low-inclined signals. Hence, back azimuth estimation using the planar wave propagation approximation can be carried out in the horizontal plane only. Metz et al. (2018) have indicated a systematic back azimuth bias of $-1.3^\circ \pm 0.2^\circ$ for H03S, resolved by estimating the back azimuth of repetitive airgun shots near the coast of Chile.

2.2. Broadband Three-Component Seismometers

We limit broadband seismic stations up to 2,000 km from the MVC source. More distant seismic stations suffer from too high ambient noise levels (Metz et al., 2016). Metz et al. (2016) use the vertical component of a broadband seismic station on Rarotonga as the near-source reference. The particular time series has the SEED-ID *IU.RAR.00.BHZ*. The location code 00 corresponds to a Geotech KS-54000 borehole seismometer sampling at 20 samples-per-second (sps). The seismometer has a non-flat passband and a complete 180° phase shift between 1 Hz and the Nyquist. Furthermore, data is only available from late 2010 until early 2018.

At Rarotonga, another higher quality Streckeisen broadband seismometer is available at location code 10. The seismometer samples at 40 Hz, has a flat-frequency response starting at 0.02 Hz and a zero-phase response above 0.2 Hz. Table 1 lists all similar and currently operational seismometers within 2,000 km of the MVC. Recently, an even higher sampled channel of 100 Hz became available, for example, *HHZ*, the so-called high broadband seismometer. Unfortunately, the initial data availability and total duration do not apply yet.

Note that the last character of the SEED-ID's channel code indicates the data orientation. A positive voltage on the digitizer channel means the ground moved in the given direction. The seismometer's orthogonal components are only represented by characters Z (vertical), N (North-South), and E (East-West) when the actual orientation is within 5° of the indicated orientation. Hence, instruments with numerical orientation codes 1 and 2 in Table 1 deviate more than 5° from north or east. The dip and azimuth fields in the metadata define the actual orientation of the seismometer.

From all considered Streckeisen seismometers (see Figure 1a), a pronounced MVC signal is only present at RAR. The instrument at NIEU observes a weaker and effectively high-pass filtered signal than RAR, likely due to the shallow depth near the source. Consequently, cross-correlations of NIEU and H03S contain only energy above 6 Hz. Due to severe blockage, no MVC signal is observed on the seismometers at AFI, RAO, and NFK. Source-receiver depth profiles with cross-track variations for the considered instruments are given in Figure S5 in Supporting Information S1. Broadband seismometers located in Fiji have a clear line of sight but are not publicly available. Therefore, in the remainder of this study, we only consider the three-component Streckeisen seismometer at Rarotonga with SEED-IDs *IU.RAR.10.BH[1,2,Z]*.

3. Pre-Processing of Raw Recordings

Pre-processing the raw recordings matches instrument sensitivity and sample rate differences while preserving as much phase and spectral information as possible for the cross-correlation analysis. There is no common denominator between the hydrophone and seismometer sample rates, of 250 and 40 sps, respectively. Hence, a sample rate of 50 sps facilitates the cross-correlation of hydroacoustic and T-phase observations.

The following time series operations of ObsPy (Beyreuther et al., 2010) are sequentially applied given the data's channel code. In all three workflows, the time window is extended symmetrically as such that signal processing artifacts like, for example, filtering; do not affect the desired time window. Total data availability for the extended time window is required. We discard the time window if any sample is missing. The minimal and average annual time window availability equal 98.9% and 99.7%, respectively.

In the case of 100 sps high broadband seismometer data, a simple decimation applied before the instrument response removal replaces the resampling steps by interpolation and the corresponding low-pass anti-aliasing filter, similar to the hydroacoustic data workflow. Avoiding interpolation improves the quality and reduces the computational effort significantly. The higher sampling rate, however, extends the frequency range beyond the 18–30 Hz band of whale vocalizations, which can last for extended periods of time. In this study, the useful seismometer data frequency range is limited below 20 Hz and so below the whale vocalizations band.

Listed filters in the following processing sequences are all zero-phase second-order Butterworth filters applied in the time-domain.

3.1. Channel BH[Z,R,T]—Broadband Seismometer Particle Velocity

1. select the time window, extended at both sides by 5% of its length
2. demean
3. filter by a 0.5 Hz high-pass
4. instrument response removal with output particle velocity
5. rotate the orthogonal components to the true ZNE
6. rotate the horizontal components toward the MVC (NE → RT)
7. select the component of interest: vertical (channel = BHZ), radial (channel = BHR), or transverse (channel = BHT)
8. upsample to 50 sps by Lanczos interpolation ($\alpha = 20$)
9. filter by a 20 Hz low-pass to minimize interpolation artifacts (anti-aliasing filter)
10. trim to the desired time window
11. demean
12. cosine taper at both sides by 5% of its length with a maximum of 30 s

3.2. Channel EDH—High Broadband Hydroacoustic Pressure

1. select the time window, extended at both sides by 5% of its length
2. demean
3. filter by a 0.5 Hz high-pass
4. decimate with a factor 5–50 sps (including a 25 Hz anti-aliasing filter)
5. instrument response removal
6. trim to the desired time window
7. demean
8. cosine taper at both sides by 5% of its length with a maximum of 30 s

4. Cross-Correlation Functions

CCFs are obtained by the linear unbiased digital cross-correlation after Bendat and Piersol (1987); and cross-correlation is applied in the frequency domain. Consider two receivers i and j at locations \mathbf{x}_i and \mathbf{x}_j with time-domain recordings $y_{i|t}(s)$ and $y_{j|t}(s)$ centered around absolute time t with duration T and relative time $s = [0, T]$. We denote $\phi_{i,j}$ the horizontal azimuth or absolute bearing angle of the vector pointing from \mathbf{x}_i to \mathbf{x}_j , measured clockwise from north, and $d_{i,j}$ the corresponding geodetic distance. The recordings are pre-processed according to Section 3 and hence both sample the wavefield at f_s sps with the total number of samples $n = Tf_s$. The time-domain cross-correlation as a function of time lag τ is then defined as,

$$C_{i,j|t}(\tau) = \frac{1}{2T} \int_{-T}^T y_{i|t}(s) y_{j|t}(s + \tau) ds. \quad (1)$$

Hence, a signal recorded at \mathbf{x}_j prior to the time of recording at \mathbf{x}_i will peak at a positive time lag, whereas a signal passing \mathbf{x}_j before \mathbf{x}_i will peak at a negative time lag. Let \mathcal{F} be the forward Fourier-transform and \mathcal{F}^{-1} its inverse. Then, the frequency domain representations of $y_{i|t}$ and $y_{j|t}$ yield $Y_{i|t}(\omega) = \mathcal{F}\{y_{i|t}(s)\}$ and $Y_{j|t}(\omega) = \mathcal{F}\{y_{j|t}(s)\}$, respectively. The pre-processed time-domain recordings $y_{i|t}$ and $y_{j|t}$ are zero-padded up to $2 \times n - 1$ samples to avoid phase wrapping artifacts arising for large frequency lags. We define the frequency domain cross-correlation, that is, the cross-spectrum as a function of frequency lag ω ,

$$\hat{C}_{i,j|t}(\omega) = \mathcal{F}\{C_{i,j|t}(\tau)\} = Y_{i|t}^*(\omega) Y_{j|t}(\omega). \quad (2)$$

The superscript-asterisk $*$ denotes the complex conjugate. Hence, the (time-domain) cross-correlation becomes a multiplication in the frequency domain. The unbiased and normalized digital cross-correlation as a function of time lag τ becomes,

$$\tilde{C}_{i,j|t}(\tau) = \frac{w(\tau)}{\|y_{i|t}\| \|y_{j|t}\|} \cdot C_{i,j|t}(\tau) = \frac{w(\tau)}{\|y_{i|t}\| \|y_{j|t}\|} \cdot \mathcal{F}^{-1}\{\hat{C}_{i,j|t}(\omega)\}. \quad (3)$$

The normalized correlation coefficient takes range between -1 (perfect anti-correlation) and $+1$ (perfect correlation), with 0 representing no correlation. Bias correction by $w(\tau)$ is required to account for the decreasing number of samples with increasing time lag. Without correction, the CCF has a typical cigar-like shape with decreasing amplitude for large time lags, or a triangle in case of correlating energy. The digital cross-correlation is unbiased by the following more intuitive time-domain representation of the weights,

$$w(\tau) = \frac{n}{n - |\tau|f_s}. \quad (4)$$

For small time lags the weights are approximately linear.

Cross-correlation corresponds to a directional estimate given a plane wave signal. A zero time or phase lag corresponds to an arrival orthogonal to the receiver pair, regardless of the true phase velocity of the signal. A signal propagating along the receiver path yields a peak time lag proportional to the geodetic distance $d_{i,j}$; and inversely proportional to the phase velocity. For any other direction, phase velocity retrieval from time lag is ambiguous. For a known source, the phase velocity can be estimated from the time lag; which is proportional to the relative geodetic distance with respect to the source location, $d_{i,j}^s = d_{i,s} - d_{j,s}$. In practice, the estimated phase velocity is neither exact nor free from error, for example, due to source location uncertainty and variability or spurious events. In the interest of a known source, however, the corresponding *signal* time lags can be obtained from the relative geodetic distance given an expected phase velocity range.

4.1. Implementation

For H03S and RAR, the average relative distance to the MVC yields 7,308.1 km (Table 2). Assuming SOFAR channel propagation ($1,450$ – $1,520$ m s^{-1}), the signal time lag bounds denote 4,872.1 and 5,005.5 s (~ 1.4 hr). Cross-correlation windows have a 24 hr duration with 3 hr increments (21 hr overlap). A long time window is preferred to suppress noise and undesired events like earthquakes while maximizing the MVC signal contribution. Maximum performance is obtained when the time window closely bounds the MVC activity. Additionally,

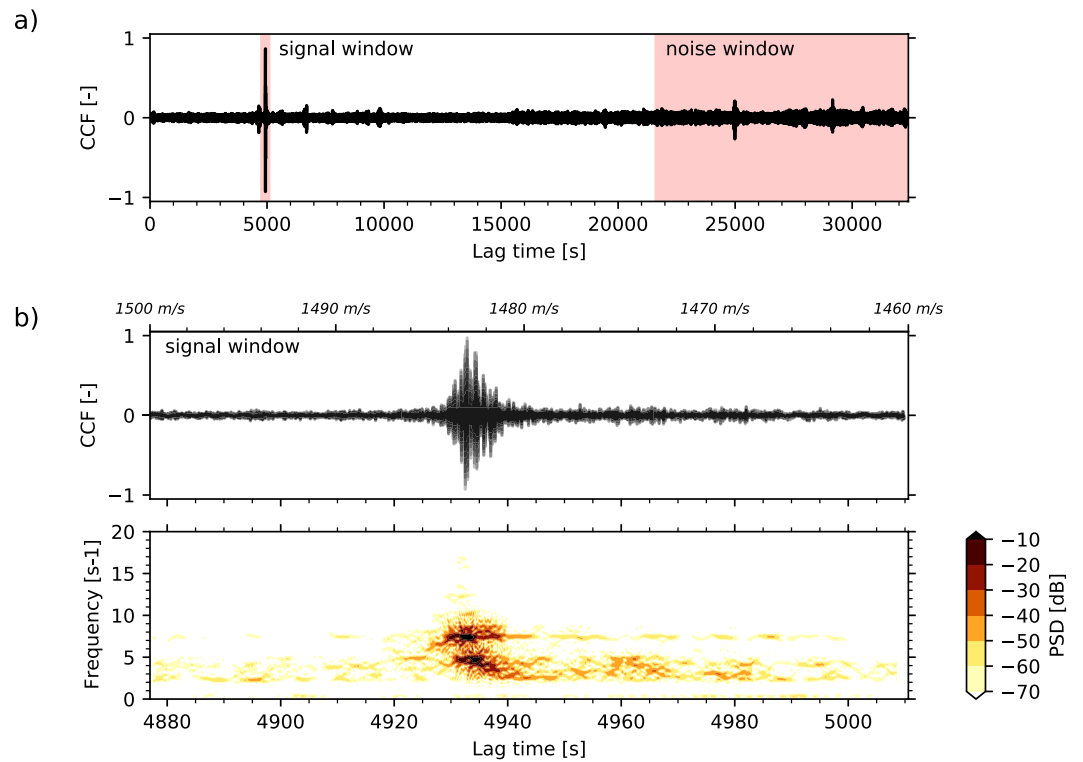


Figure 2. Cross-correlation function (CCF) between *IM.H03S1..EDH* and *IU.RAR.10.BHZ* for 15 January 2015 (unbiased, demeaned, high-pass filtered with a zero-phase 2nd order Butterworth filter with a 3 Hz corner frequency, and normalized). Start and end times of the signal- and noise windows in (a) correspond to values indicated in Section 5.1. (b) Zoom-in on the signal window (top) and the corresponding spectrogram (power spectral density) for 2.5 s subwindows with a padding factor of 4 (bottom). Indicated velocities correspond to the time lag and the relative distance between the two receivers using Table 2.

we choose the duration and increment such that both agree with the time lag of interest (Bendat & Piersol, 1987; Groos, 2010). The recommended rule-of-thumb states that: (a) time lags of interest should exceed 20% of the window duration in order to minimize CCF artifacts, and (b) the time-window increment should approximately equal the time lag of interest in obtaining proper sampling over time. The 3 hr increment is chosen to limit the computational effort. To limit data storage, we trim the CCF to the single-sided time lags, from 0 to 12 hr, of the same sign as the signal window. Furthermore, the subsample time offsets between the actual start time of y_{jlr} and y_{jlr} and the desired CCF start time are stored. These minor timing errors are corrected in post-processing by time-shifting the CCF.

4.2. Example CCF

An example CCF between *IU.RAR.10.BHZ* and *IM.H03S1..EDH* is shown in Figure 2 for 15 January 2015. The CCF is unbiased, demeaned, and high-pass filtered by a zero-phase second-order Butterworth filter with a 3 Hz corner frequency. Figure 2b zooms in on the signal window. Time lag and indicated velocity at the peak CCF corresponds to the SOFAR channel speed of sound. The spectrogram shows a modal propagation signature similar to the study of (e.g., Evers et al., 2017) with the expected SOFAR channel dispersion: high-frequency modes are more narrowly confined to the SOFAR channel axis and therefore arrive before the lower-frequency modes (Munk, 2006). Given a stationary and comparable source, the phase-velocity dispersion curve could be retrieved similar to Kästle et al. (2016). Despite the clear modal signature in Figure 2b, the MVC is not a perfect stationary source with an identical signature for each event (e.g., Metz et al., 2018).

Figure 3 shows the CCFs between the vertical and radial component at RAR with the hydrophone triplet of H03S. The CCF time-window and post-processing is similar to Figure 2. The CCFs with each of the three hydroacoustic sensors exhibit a very similar signature, with near-identical velocities at the peak correlation. Inter-element time

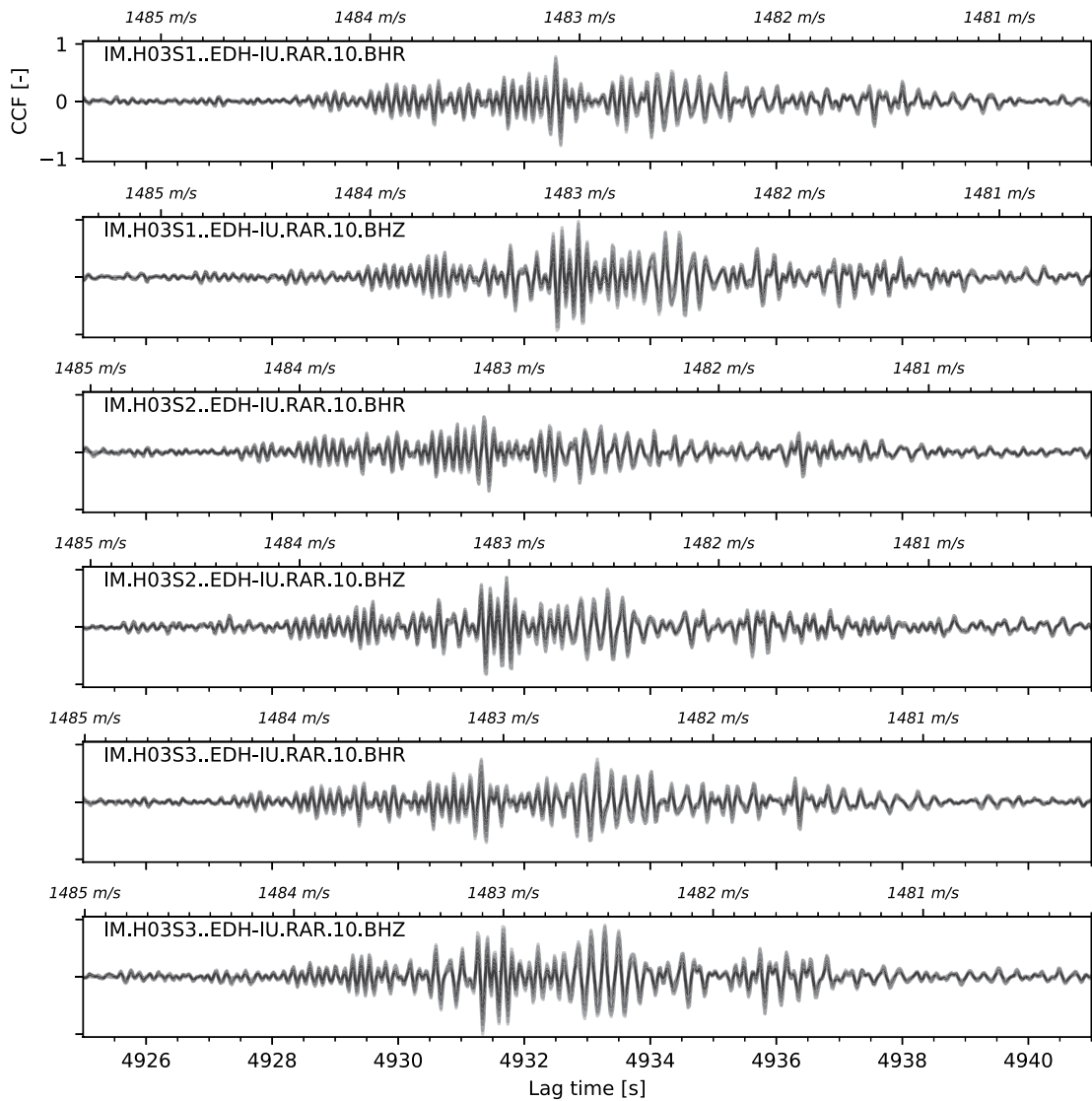


Figure 3. Cross-correlation functions (CCFs) between RAR and H03S for 15 January 2015 (unbiased, demeaned, high-pass filtered with a zero-phase second-order Butterworth filter with a 3 Hz corner frequency, and normalized). All eight CCFs with 3 hr increments corresponding to the same day are plotted on top of each other. Indicated velocities correspond to time lag and the relative distance for the given receiver pair using Table 2.

lag differences of the CCFs are used to verify the direction of the MVC source assuming a planar wave propagating across the hydrophone triplet (see Section 5.2).

In the following, MVC CCFs between H03S and RAR are estimated for six different receiver couples, that are, *IM.H03S[1–3]..EDH-IU.RAR.10.BHZ* and *IM.H03S[1–3]..EDH-IU.RAR.10.BHR*. The period spans from April 2014 until 2020.

5. Systematic CCF Selection

Systematic selection of eligible CCF is required to account for the non-continuous source and spurious events. CCFs eligible for time-lapse analysis are selected based on: (a) source activity and (b) source directionality. Source activity (Section 5.1) is determined by the signal-to-noise ratio of the CCFs assuming sound propagation through the SOFAR channel. Active periods are automatically extracted by a coincidence-trigger analysis for which all six receiver couples should exceed a prescribed threshold. Source directionality (Section 5.2) is retrieved from the inter-element time-delays of the CCFs assuming a plane wave traversing the hydrophone

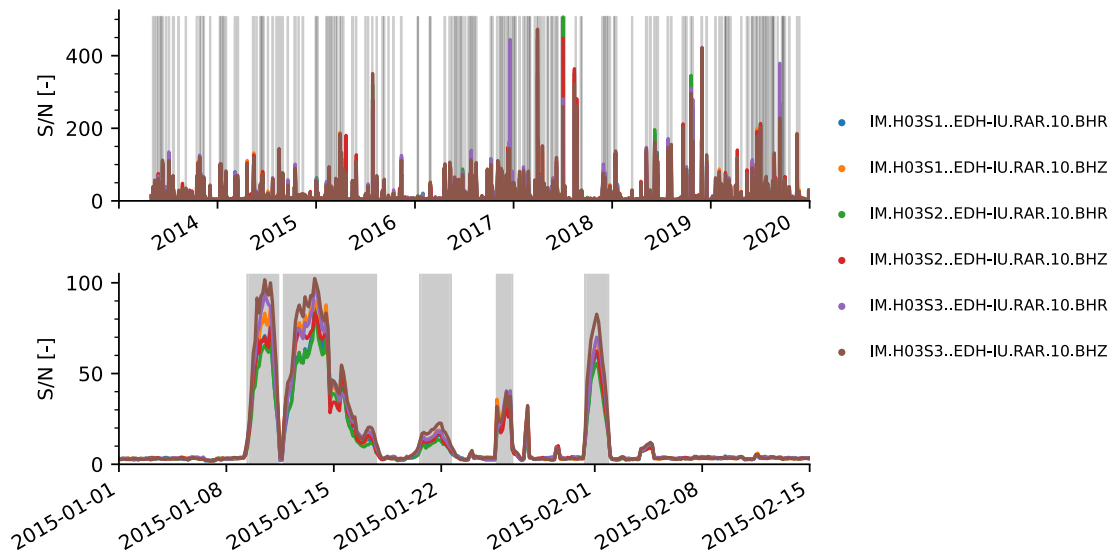


Figure 4. Signal-to-noise ratio (a measure of the MVC source activity) for 2014–2020 (top) and a zoom-in on a 1.5 months active period (bottom) containing the example cross-correlation functions (CCFs) of Figures 2 and 3. Eligible source activity is indicated in gray and corresponds to coincidence triggered periods with an S/N threshold of 10 and a minimum duration of one day.

triplet. Only CCFs of the hydrophone triplet with the vertical seismic component are used to estimate the back azimuth.

5.1. Source Activity Estimation

Signal-to-noise ratio (S/N) of a CCF is defined as,

$$S/N_{i,j|t} = \frac{\max \left(\left| \tilde{C}_{i,j|t}(\tau_{\text{signal}}) \right| \right)}{\text{RMS} \left(\tilde{C}_{i,j|t}(\tau_{\text{noise}}) \right)}, \quad (5)$$

with τ_{signal} and τ_{noise} the time lags for signal and noise windows, respectively. The unbiased CCF is demeaned and filtered with a 3 Hz high-pass (zero-phase 2nd order Butterworth).

- **Signal window:** time lags proportional to the velocity range for SOFAR channel propagation (1,450–1,520 m s⁻¹) along with the relative distance between the two receivers and the source (~7,308.1 km)
- **Noise window:** 6–9 hr posterior time lags with the same sign as the signal window

“Source activity” is defined as a period for which the S/N of six CCFs exceed the prescribed threshold of 10 and which has a minimum duration of one day (one cross-correlation window). Figure 4 indicates the estimated source activity periods for 2014–2020. Figure 5 gives the corresponding yearly metrics. Note that year 2014 starts from May due to data unavailability of H03. The activity distribution over the years is relatively uniform; the activity distribution during the year is not. Non-uniform sampling can affect the estimation of periodic signatures, such as seasonality, in the time-lapse analysis.

Activity estimation, including the cross-correlations with the radial component, is essential to (a) increase the number of observations and (b) reduce falsely triggered periods. Figure 6 demonstrates that the time lag of the peak amplitude is not robust, even applying it to the envelope for eligible MVC activity only. Minor differences in time lag are likely related to cycle skipping, whereas large jumps correspond to different modal peaks attributed to variations in the source signature, for example, the spectral response or the acoustic to seismic conversion. Hence, utilizing the peak amplitude time lag will make acoustic thermometry erratic.

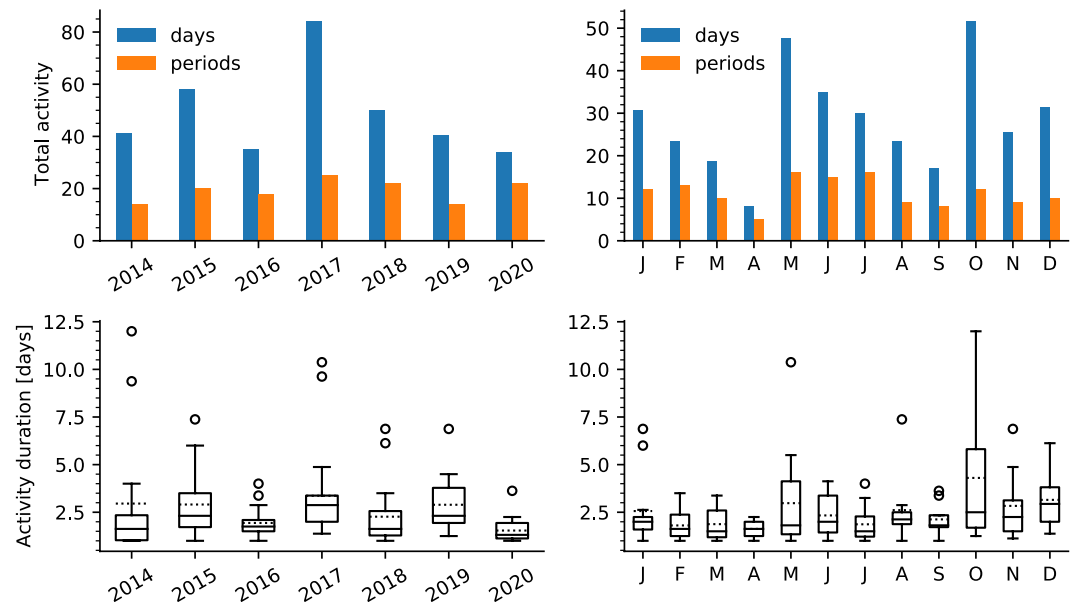


Figure 5. Estimated source activity per year (left) and per month (right). Note that year 2014 starts from May due to data unavailability of H03. (top) Total activity in terms of days and triggered continuous periods per year and per month. (bottom) Box-and-whiskers plots of the activity duration. The box indicates the inner quartile range (IQR, the 75% quartile minus the 25% quartile) with the horizontal lines representing the median (solid) and the mean (dashed), respectively. The whiskers indicate the range and extend no more than $1.5 \times$ IQR from the edges of the box. Values outside this range are represented by black circles.

5.2. Source Directionality Estimation

Consider a source at a considerable distance from the hydrophone triplet array. If the curvature of the wavefront over the array's aperture is sufficiently small, then the wavefront can be approximated locally by a propagating planar wave. The estimation of the direction of propagation of the plane wave is carried out in the horizontal plane only under the assumption that the vertical extent of the triplet has a negligibly small contribution to the observed time delays (Edwards & Green, 2012). Then, the plane wave is described by the horizontal slowness vector s ,

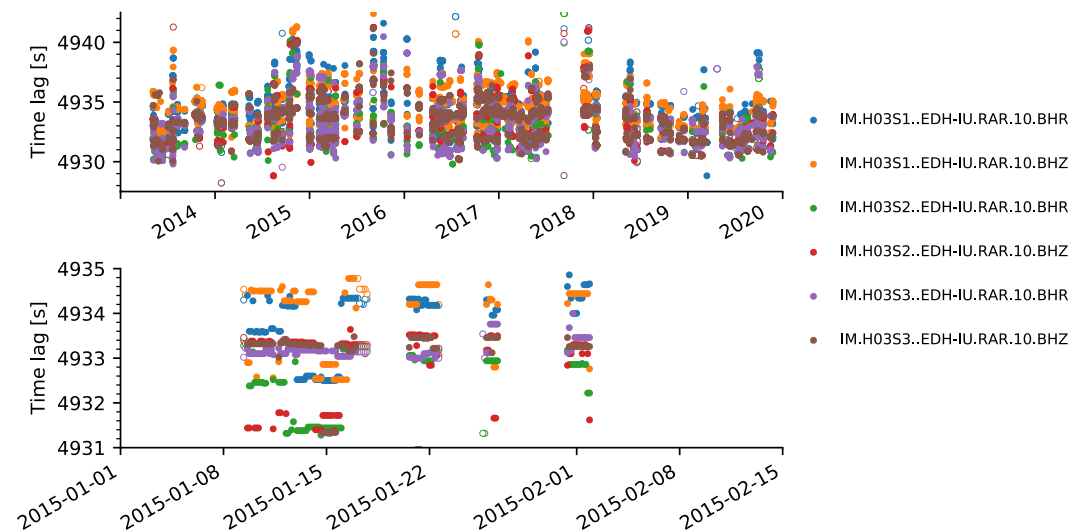


Figure 6. Time lag associated with the peak envelope correlation-coefficient for eligible source activity only. (top) Entire period and (bottom) zoom-in for the similar period as in Figure 4. Empty circles correspond to invalid plane wave characteristics. The resolved time lag is not robust and should not be used for thermometry.

characterized by the back azimuth angle or direction of arrival ϕ_b and the horizontal propagation velocity v_H across the array.

We estimate the horizontal slowness vector by least squares fitting a plane wave traversing the hydroacoustic triplet using the CCFs of the three acoustic channels with either the vertical or radial component of the seismic station. If the expected source activity is genuinely associated with the MVC, then the estimated slowness vector \mathbf{s} should direct toward the source with a local horizontal velocity greater or equal than the local SOFAR channel propagation velocity.

Consider an array of N receivers located in a horizontal plane at $\mathbf{r}_i = (x_i, y_i)$ for $i = 1, N$. Then, the time lag of arrival of the wave at a receiver yields $\tau_i = \mathbf{s} \cdot \mathbf{r}_i$, referred to some arbitrary time. For $\Delta z_i \approx 0$ it holds that $|s_z r_z| \ll |s_x r_x + s_y r_y|$, hence, the z -coordinate can be ignored. The array will have a set of $M = N(N - 1)/2$ non-redundant receivers couples, the *co-array*. The plane wave will arrive at the co-array according to (e.g., Bishop et al., 2020; Szuberla & Olson, 2004),

$$\boldsymbol{\tau} = \mathbf{X}\mathbf{s} + \boldsymbol{\epsilon}, \quad (6)$$

with,

$$\boldsymbol{\tau} = \begin{pmatrix} \tau_1 \\ \tau_2 \\ \vdots \\ \tau_M \end{pmatrix}, \quad \mathbf{X} = \begin{pmatrix} \Delta x_1 & \Delta y_1 \\ \Delta x_2 & \Delta y_2 \\ \vdots & \vdots \\ \Delta x_M & \Delta y_M \end{pmatrix}, \quad \mathbf{s} = \begin{pmatrix} v_H^{-1} \sin \phi_b \\ v_H^{-1} \cos \phi_b \end{pmatrix},$$

where $\boldsymbol{\tau}$ is the vector of receiver couple delay times, \mathbf{X} the receiver couple offset matrix, \mathbf{s} is the horizontal slowness vector, and $\boldsymbol{\epsilon}$ is the vector of timing errors. It is assumed that $\boldsymbol{\epsilon}$ is normally distributed with zero-mean and variance σ^2 (Szuberla & Olson, 2004). The ordinary least squares estimate of the overdetermined system for \mathbf{s} becomes,

$$\hat{\mathbf{s}} = (\mathbf{X}^T \mathbf{X})^{-1} \mathbf{X}^T \boldsymbol{\tau}, \quad (7)$$

with minimum value of the error,

$$R_0^2 = (\boldsymbol{\tau} - \mathbf{X}\hat{\mathbf{s}})^T (\boldsymbol{\tau} - \mathbf{X}\hat{\mathbf{s}}). \quad (8)$$

Inter-element delay times $\boldsymbol{\tau}$ of the triplet are retrieved by cross-correlation, or in our case by cross-correlation of the CCFs signal windows, and correspond to the time lag associated with the peak correlation coefficient. The inter-element time-delays are noticeable in the CCFs in Figure 3 for 15 January 2015. Figure 7 shows the estimated horizontal slowness components for the vertical seismic component, whereas Figure 8 shows the corresponding direction of arrival and the horizontal propagation velocity as a function of time. Results for the radial seismic component are comparable and are provided as Figures S1 and S2 in the Supporting Information S1. The slowness vectors associated with MVC activity cluster around the slowness values one would expect for a signal originating at the MVC. The difference between the estimated plane wave bearing and the actual bearing (see Table 2) closely approximates the expected back azimuth error of -1.3° (see Section 2.1 and Metz et al., 2018). The horizontal velocity close to the local sound speed indicates a near-horizontal propagation in the SOFAR channel. Activity-based filtering discards most other hydroacoustic and seismic events.

Note that the reduced 50 Hz sampling rate affects the precision of $\boldsymbol{\tau}$ and so the estimated horizontal slowness. The lack of a single resolved azimuth and velocity can be explained by the fact that: (a) the MVC is not a single point source (Metz et al., 2018), (b) the medium is horizontally reflective, refractive, and diffractive (Jensen et al., 2011), and (c) the hydrophone triplet is moored vertically only: sensor locations slightly vary over time due to the streaming of the water (Nichols & Bradley, 2017).

Estimated plane wave characteristics are an additional selection criterion besides the activity estimation for extracting eligible CCFs for the time-lapse analysis. Plane wave characteristics take range 241° – 243° and

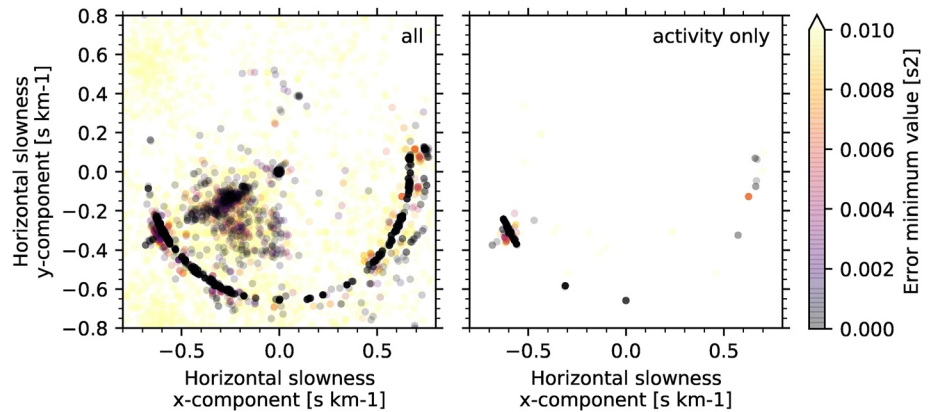


Figure 7. Plane wave estimations using the cross-correlation function (CCF) signal windows for the correlations of *IM..H03S[1–3].EDH* with *IU.RAR.10.BHZ* for (left) the entire period 2014–2020 and (right) CCFs with S/N triggered activity only. Take into account that density information of the plotted plane wave characteristics is limited. See Figure 8 for representative density information.

1,490–1,495 ms^{-1} , for the direction of arrival and local horizontal velocity, respectively, with a maximal error of $R_0^2 < 0.02$.

6. Time-Lapse Analyses

Time-lapse cross-correlation analysis is applied to eligible CCFs to extract relative travel time variations. Eligible CCFs fulfill both the source activity (see Section 5.1) and the horizontal slowness (see Section 5.2) criteria.

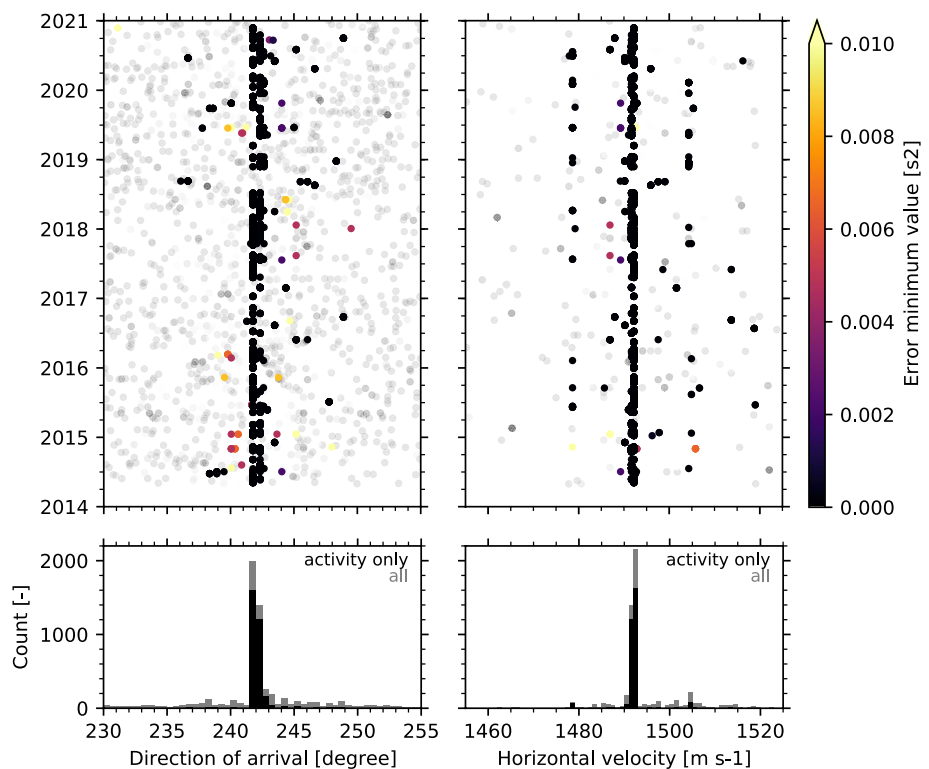


Figure 8. Estimated plane wave characteristics as a function of time using the cross-correlation function (CCF) signal windows for the correlations of *IM..H03S[1–3].EDH* with *IU.RAR.10.BHZ*. Colored circles in the top row correspond to S/N triggered activity, whereas light-gray circles correspond to the non-triggered CCFs.

Cross-correlation can be applied to the signal windows of the eligible CCFs to obtain time lag differences between two reference times. The implementation would be precisely similar to the approach described in Section 4. However, this would only yield the resemblance between the different CCFs, the peak absolute cross-correlation coefficient, and the corresponding time lag difference. That is, source signatures variations would not be quantified intrinsically. A solution would be to filter the CCFs in very narrow frequency bands, yielding the time lag variation and resemblance per frequency. The path averaged phase-velocity dispersion curve could then be obtained by phase-tracking (e.g., Weemstra et al., 2020). Unfortunately, source activity is too sporadic resulting in relatively large travel time variations between periods of activity (see Figure 5). These significant travel time variations will cause cycle skipping and render phase tracking impossible.

Therefore, this study applies time-lapse analysis to the spectrograms (S) of the eligible CCFs signal windows and yields the variation in travel time, on the one hand, and quantifies the variation in source signature on the other. Two discrete frequency bands are used, of 3–6 Hz and 6–12 Hz, which contain the two modal peaks (see Figure 2). First, we process the unbiased CCF as follows:

1. extract the signal time lags of interest
2. demean
3. cosine taper with a 5 s duration to suppress FFT artifacts
4. time shift by FFT resampling as such that the first sample exactly matches the start time of the CCF window
5. high-pass filter in the time-domain with a zero-phase fourth-order Butterworth filter with a 1.5 Hz corner frequency
6. cosine taper with a 1.5 s duration to remove filter artifacts at the edges

Then, we compute the spectrogram in terms of the power spectral density using consecutive short-time Fourier transforms (STFTs). Subwindows have a duration of 2.5 s with a padding factor of 4 and are time-shifted exactly one sample. The CCF sampling frequency of 50 sps is preserved. The frequency resolution equals 0.1 Hz (one divided by the Fourier transformed time window). A Tukey window suppresses spectral leakage. Finally, the spectrogram is split in the two consecutive octaves Θ_1 and Θ_2 , containing spectral content from 3 to 6 and 6 to 12 Hz, respectively.

The time-lapse analysis is applied per receiver pair by two-dimensional normalized cross-correlation of the trimmed spectrograms $S_{i,j|t_1,t_2|\Theta}$ for all combinations of eligible time windows. The technique is related to generalized two-dimensional correlation in, for example, spectroscopy and image processing. We apply two-dimensional cross-correlation in the frequency domain, similar to the one-dimensional digital cross-correlation of Section 4. Only the absolute peak of the obtained two-dimensional cross-correlation function (2D CCF) and the corresponding time shift ($\Delta\tau$) and frequency shift (Δf) are stored,

$$\alpha_{i,j|t_1,t_2|\Theta} = \max \left| \tilde{C}_{i,j|t_1,t_2|\Theta}^S(\Delta\tau, \Delta f) \right|, \quad \Delta\tau_\alpha = \Delta\tau|_\alpha, \quad \Delta f_\alpha = \Delta f|_\alpha.$$

The characteristics as a function of receiver pair (i, j) and octave Θ , are used to track both source and medium related variations over all time combinations (t_1, t_2). Since the power spectrum is always real and non-negative, the cross-correlation of power spectra range from zero (no correlation) up to one (a perfect correlation). The lack of phase information prohibits addressing anti-correlation. The time reciprocity, given a fixed receiver pair and octave, yields,

$$\alpha(t_1, t_2) = \alpha(t_2, t_1), \quad \Delta\tau_\alpha(t_1, t_2) = -\Delta\tau_\alpha(t_2, t_1), \quad \Delta f_\alpha(t_1, t_2) = -\Delta f_\alpha(t_2, t_1).$$

The raw time-lapse results, including all time combinations, are given in Figures B1 and B2 for the 3–6 and 6–12 Hz octave bands, respectively. The filtered time-lapse results for spurious time steps are given in Figures 9 and 10. $\alpha_{i,j|t_1,t_2|\Theta}$ is designated as spurious if it is anomalously low compared to adjacent α 's. This can be recognized by the low-valued rows and columns in, for example, Figure B1 for α . Identifying such rows and columns yields the non-eligible time combination at their intersection. Specifically, we exclude non-eligible time combinations by use of the *trimean* (or Trimean, see Appendix A), a robust and resistant measure of central tendency including information of the magnitude of the data compared to the median.

A non-eligible time step of a pair is quantified by $\text{Trimean}(\alpha_{i,j|t_1,t_2=|t|\Theta}) \leq 0.5$, that is, an average peak correlation value never better than tossing a coin. Hence, we qualify an eligible time step as one for which all pairs are greater

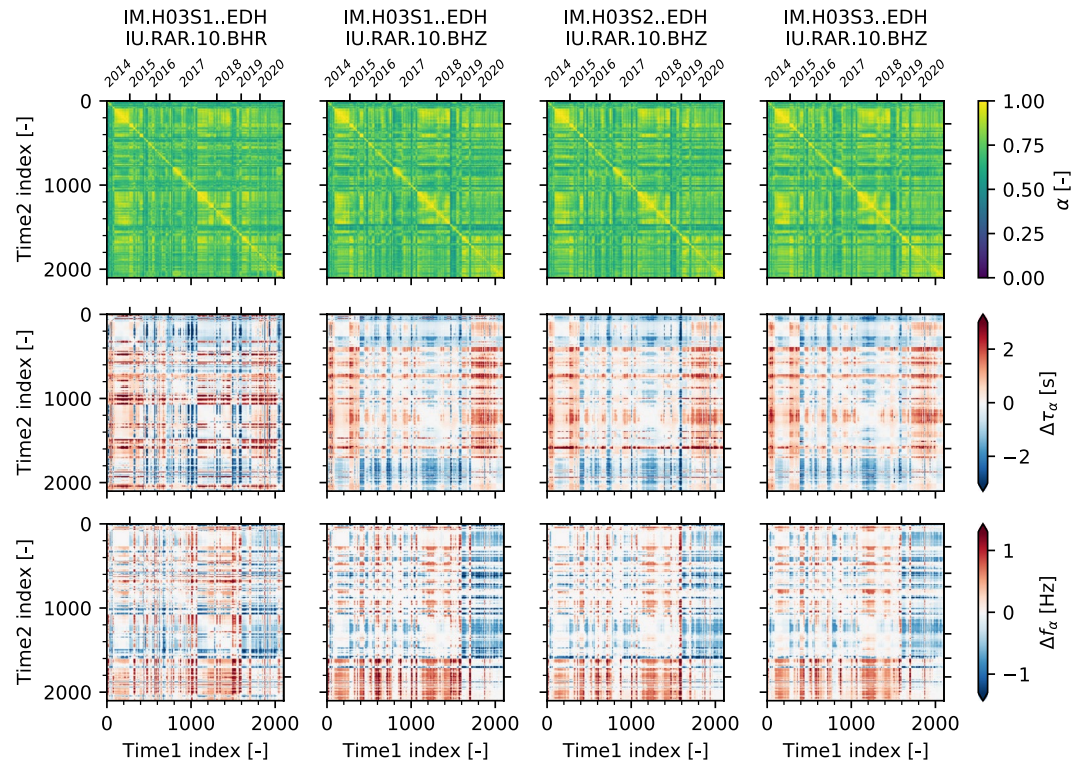


Figure 9. Time-lapse results for the 3–6 Hz octave band, filtered for spurious time combinations. The relative time index indicates the integer position for the discontinuous times t_1 and t_2 (after filtering) and takes range from 0 to 2,101. The corresponding year is indicated at the top of each frame. Unfiltered results are shown in Figure B1.

than this threshold. Furthermore, the frequency shift between spectrograms is capped using the bandwidth (f_{bw}) of the octave, $\text{Trimean}(\Delta f_\alpha) < f_{bw}/4$. From the 2,794 considered time steps, 2,102 (75.2%) and 2,092 (74.9%) are qualified, for the 3–6 and 6–12 Hz octave bands, respectively. Trimean distributions of α and corresponding Δf_α and $\Delta \tau_\alpha$ for all time-lapse pairs are given in Figures C1–C3.

The time-lapse performance of the two octave bands differs between the vertical- and radial-component α . For the 3–6 Hz octave band, the radial component yields a lower overall peak correlation coefficient α and larger variations of both Δf_α and $\Delta \tau_\alpha$ compared to the vertical component. However, for the 6–12 Hz octave band, the relation is opposite.

7. Travel Time as a Proxy for the Deep-Ocean Temperature

An acoustic signal samples the deep ocean along its path as a function of range and depth, represented by the sensitivity kernel, and yields an integrated response in terms of the travel time. Frequency dependence is important as low-frequency modes span a larger portion of the water column than higher frequencies. The travel time changes primarily depend on changes in the deep-ocean temperature (Munk, 2006). Fluctuations due to salinity or due to Doppler shifts by currents are negligible (Dushaw et al., 2009). As such, travel time changes chiefly result from path averaged temperature changes assuming no variation in the modal structure, neither due to the medium nor to the source. Inversion of travel time changes for a temperature change is explained by, for example, W. Wu et al. (2020), and is not carried out in this study. Full waveform inversion techniques are more applicable in case of a non-negligible change in the modal structure related to the velocity profile and thus temperature.

Let $\bar{\Delta \tau}_\alpha$ denote the weighted mean variation in time lag as a function of receiver pair and octave. $\bar{\Delta \tau}_\alpha$ is assumed to be equivalent to the medium induced travel time change over time, obtained from the time-lapse results of Section 6 per octave frequency band and assuming no variation of the source signature. The source's modal resemblances are quantified by $\alpha_{i,j|t_1,t_2|@}$ whereas the associated frequency variations are indicated by Δf_α .

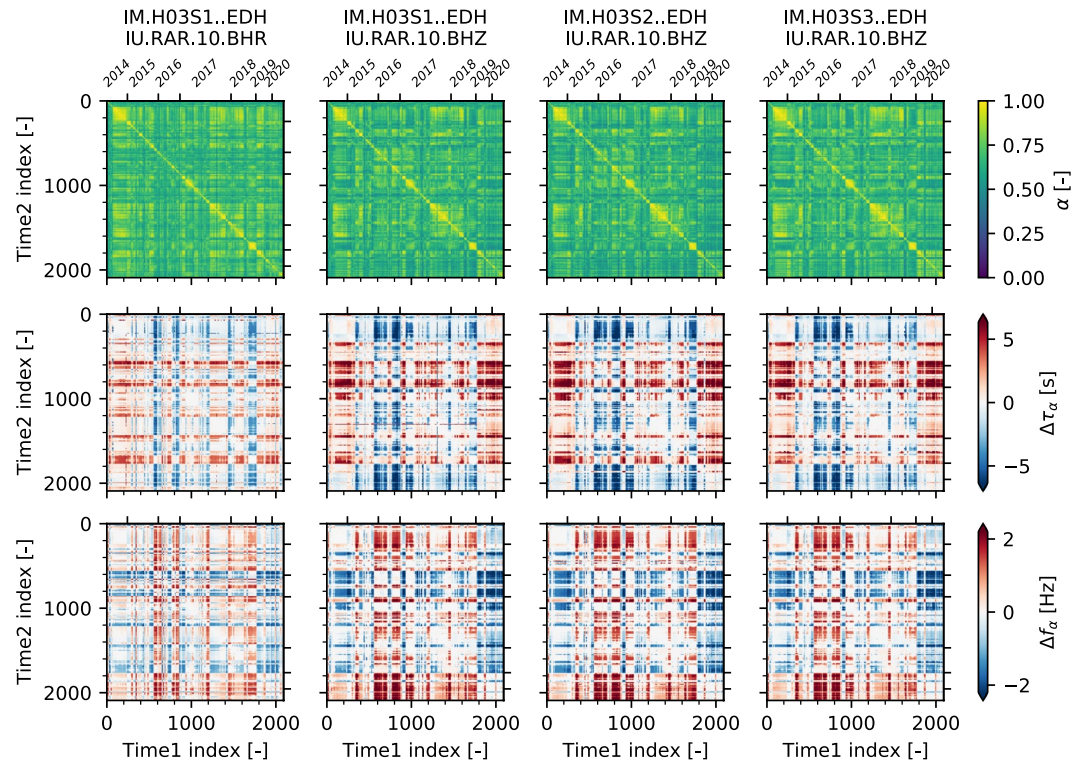


Figure 10. Time-lapse results for the 6–12 Hz octave band, filtered for spurious time combinations. The relative time index indicates the integer position for the discontinuous times t_1 and t_2 (after filtering) and takes range from 0 to 2,091. The corresponding year is indicated at the top of each frame. Unfiltered results are shown in Figure B2.

The trimmed time lag variation is weighted by the peak two-dimensional cross-correlation coefficient ($\alpha_{i,j|t_1,t_2|\theta}$) and the frequency variation Δf_α assuming a normal distribution with location $\mu_{\Delta f}$ and standard deviation $\sigma_{\Delta f}$. Hence, the weight becomes,

$$w_{\Delta\tau} = \alpha \exp\left(-\frac{1}{2}\left(\frac{\Delta f_\alpha - \mu_{\Delta f}}{\sigma_{\Delta f}}\right)^2\right), \quad (9)$$

taking values from zero up to one. For each time step, pair and octave band, the trimmed weighted mean variation in lag time is determined with the corresponding 95% confidence indicative of the uncertainty. Trimmed subsets are confined by the 0.02 and 0.98 percentiles to suppress outliers. The 95% confidence is based on the weighted variance and the Student's t test with one degree of freedom. Weighted numerical summary measures are described in Appendix A.

Obtained results assuming $\mu_{\Delta f} = 0$ Hz and $\sigma_{\Delta f} = 0.1$ Hz are given in Figures 11 and 12 for the 3–6 and 6–12 Hz octave band, respectively.

The travel time change over time reveals a complex periodic variation as well as a robust linear trend. Note that the non-uniform source activity throughout the year restricts the estimated trends, particularly the linear, to an approximation. Linear regression of $\bar{\Delta\tau}_\alpha$ is performed by Weighted Least Squares using Scikit-learn (Pedregosa et al., 2011) using 20,000 bootstrap estimations. The linear regressions are visualized in Figure 13 and listed in Table 3. The triplet averaged linear trends, using only the time-lapse couples with the vertical seismic component, are indicated by H03S[1–3]. Seasonal travel time variation is indicated by the Lomb-Scargle periodogram of the detrended $\bar{\Delta\tau}_\alpha$ in Figure 14. The estimated periodicity peaks near 675 days (~ 1.9 yr) for the 3–6 Hz octave whereas the 6–12 Hz octave peaks near 384 days (~ 1.1 yr).

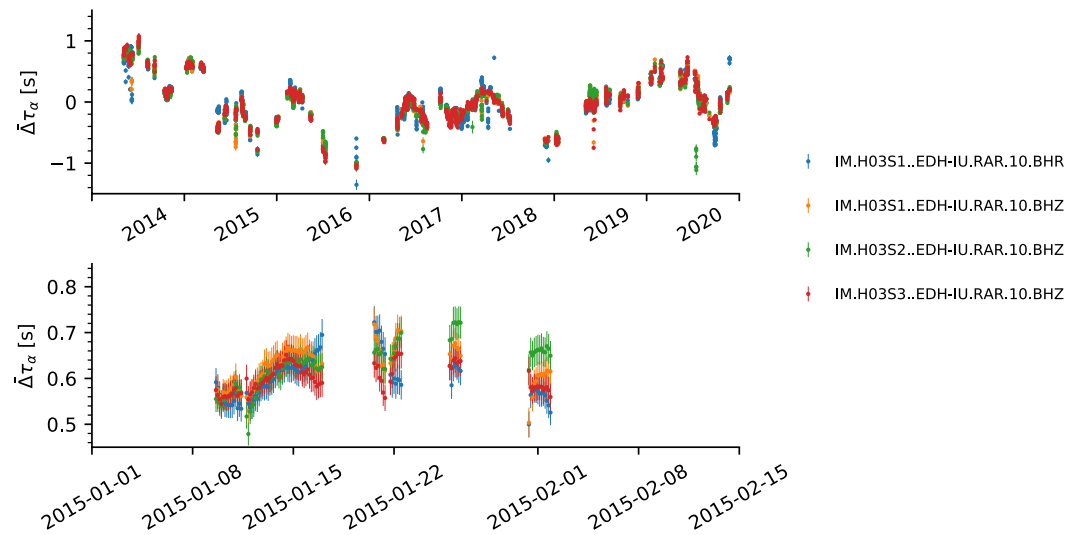


Figure 11. Trimmed weighted mean lag time variation ($\bar{\Delta}\tau_\alpha$) with the 95% confidence interval as a function of time for the 3–6 Hz octave. Trimmed subsets per time step are confined by the 0.02 and 0.98 percentiles. Time lag weights $w_{\Delta\tau}$ are defined assuming $\mu_{\Delta\tau} = 0$ Hz and $\sigma_{\Delta\tau} = 0.1$ Hz.

8. Seismometer Vertical Plane Phase Lag

CCFs of H03S1 with the rotated (i.e., radial) seismic component of RAR are analyzed to perceive the T-phase acoustic-to-seismic conversion. Acoustic-to-seismic conversion can generate two types of elastic waves: *body waves* and *surface waves* (e.g., Fowler, 2005). Body waves travel through the body of the Earth whereas surface waves are guided along the surface. Body waves usually consist of two types: primary (P or compressional) waves and secondary (S or shear) waves. Primary waves produce an alternating compressional and relaxational motion in the direction of propagation whereas secondary waves produce a shearing motion perpendicular to the direction that the wave is traveling. Hence, body waves correspond to a near-zero phase lag between the CCFs. At steep-sloped islands, such as Rarotonga, a significant amount of energy can be converted to surface shear waves (De Groot-Hedlin & Orcutt, 2000). Surface shear wave excitation strongly depends on the seafloor roughness. Surface waves are rotational waves propagating at lower velocities than those of body waves. Rayleigh surface

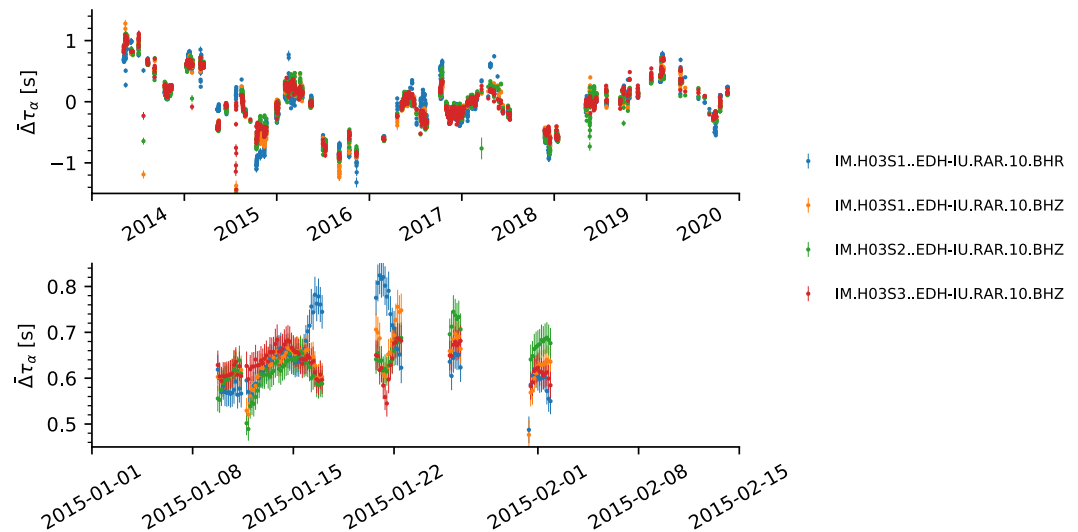


Figure 12. Trimmed weighted mean lag time variation ($\bar{\Delta}\tau_\alpha$) with the 95% confidence interval as a function of time for the 6–12 Hz octave. Trimmed subsets per time step are confined by the 0.02 and 0.98 percentiles. Time lag weights $w_{\Delta\tau}$ are defined assuming $\mu_{\Delta\tau} = 0$ and $\sigma_{\Delta\tau} = 0.1$ Hz.

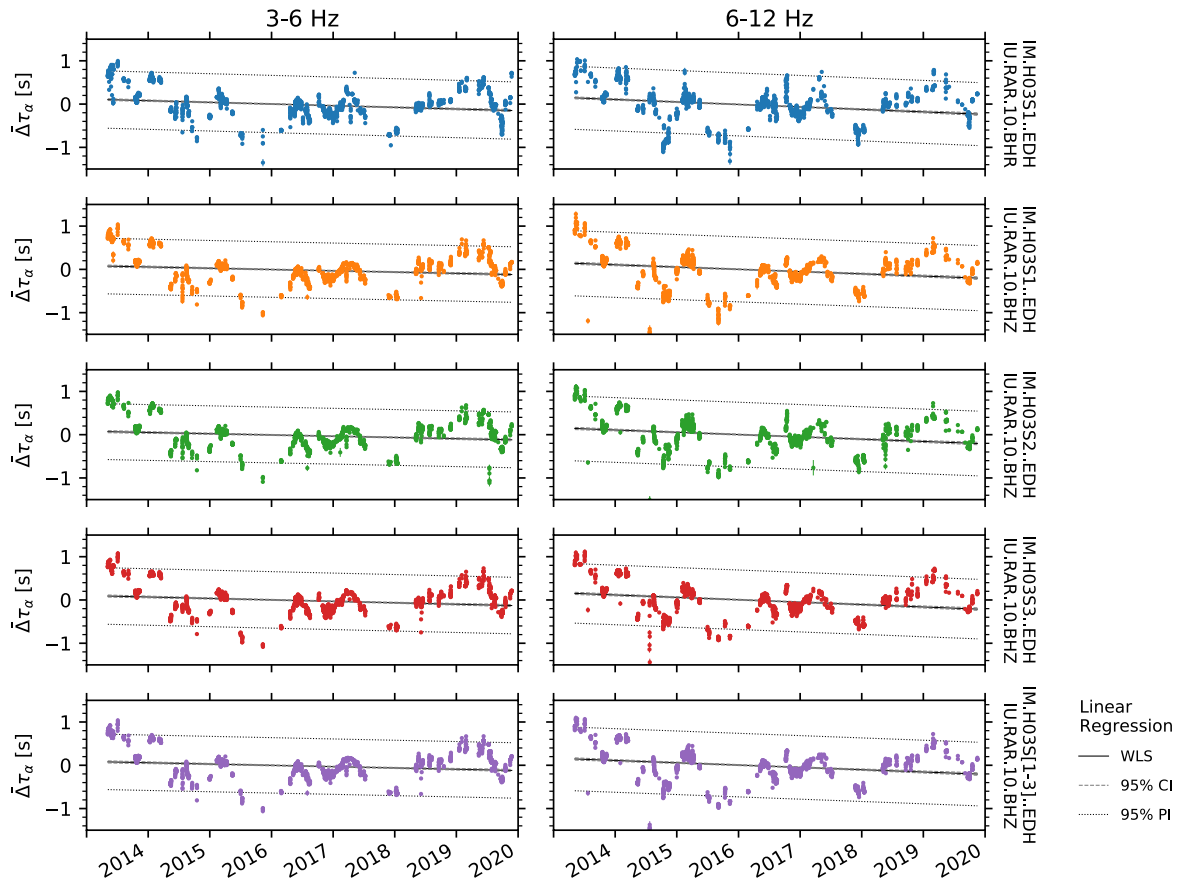


Figure 13. Trimmed weighted mean lag time variation ($\bar{\Delta}\tau_\alpha$) with the 95% confidence interval as a function of time. Trimmed subsets per time step are confined by the 0.02 and 0.98 percentiles. Sloped horizontal lines are the corresponding linear regressions (solid red line) with the 95% confidence interval (dashed blue lines, percentile distribution) and the 95% prediction interval (dashed green lines, parametric estimate) obtained from 20,000 bootstrap estimations and are listed in Table 3.

waves (LR) are characterized by an elliptical particle motion in the vertical plane. The elliptical particle motion is predominantly retrograde at the surface (Tanimoto & Rivera, 2005). The corresponding vertical plane (ZR) phase lag is approximately 90°. Love surface waves (LQ) are horizontally polarized and so would yield energy in the horizontal plane only. Love surface waves, being horizontally polarized, are not expected to couple into water column and therefore are not expected to be found in the hydrophone recordings and therefore the CCFs (Yildiz et al., 2013). The ZR phase lag of the signal-windowed CCFs of H03S1 and RAR in the vertical plane, that are, *IM.H03S1..EDH-IU.RAR.10.BHZ* and *IM.H03S1..EDH-IU.RAR.10.BHR*, is used to further distinguish

Table 3

Linear Regression of the Trimmed Weighted Mean Lag Time Variation $\bar{\Delta}\tau_\alpha$ With the Corresponding 95% Confidence Interval (Percentile Distribution, in Milliseconds Per Year) and the 95% Prediction Interval (Parametric Estimate, in Seconds) Using 20,000 Bootstrap Estimations Based on Figure 13

Pair(s)/Octave band	3–6 Hz		6–12 Hz	
	Trend ± CI [ms yr ⁻¹]	PI [s]	Trend ± CI [ms yr ⁻¹]	PI [s]
<i>IM.H03S1..EDH-IU.RAR.10.BHR</i>	-27.9 ± 2.2	0.8	-51.3 ± 2.1	0.9
<i>IM.H03S1..EDH-IU.RAR.10.BHZ</i>	-25.2 ± 3.3	0.8	-52.2 ± 4.1	1.3
<i>IM.H03S2..EDH-IU.RAR.10.BHZ</i>	-22.4 ± 3.6	0.9	-49.8 ± 3.8	1.2
<i>IM.H03S3..EDH-IU.RAR.10.BHZ</i>	-33.5 ± 4.0	0.9	-55.1 ± 4.2	1.1
<i>IM.H03S[1-3]..EDH-IU.RAR.10.BHZ</i>	-25.0 ± 3.6	0.8	-50.9 ± 3.9	1.2

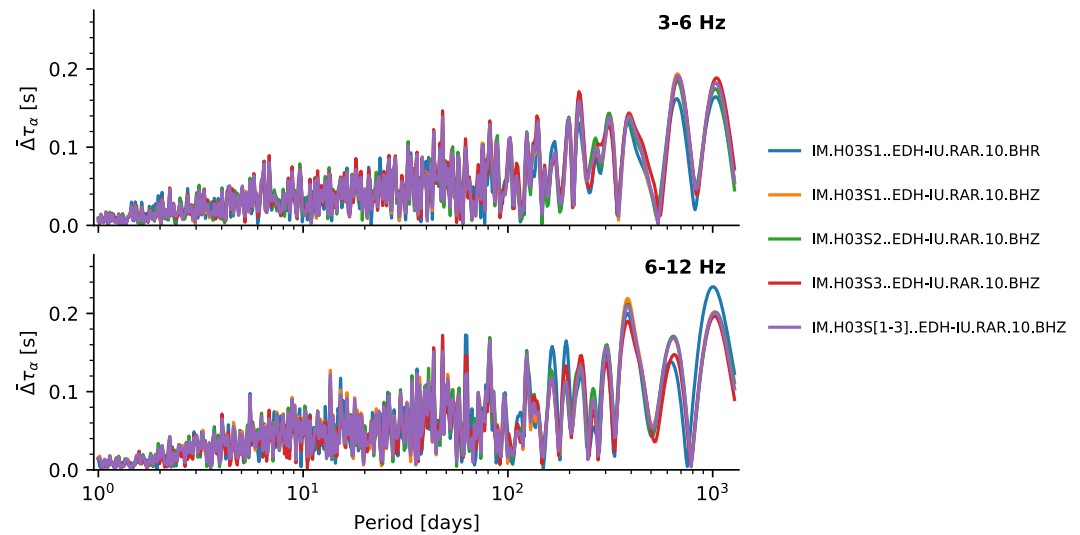


Figure 14. Lomb-Scargle periodogram based on Figure 13 after detrending by the linear regression. Periods range from 1 day to 3.5 yr.

between the aforementioned wave types. Similar phase lags densities for H03S2 and H03S3 are given in Figures S3 and S4 in Supporting Information S1. The phase lag is estimated using the cross-spectrum of Equation 2. The spectral density of the estimated ZR phase lag is given in Figure 15, for the eligible CCFs only as well as all CCFs of 2014–2020. Observed seismic wave types depend on frequency. The phase lag response indicates a mixture of dilatational body waves, at 2 and 4 Hz, for example, and rotational LQ waves, around 3 and 5 Hz. The highest ZR density corresponds to lower frequencies, up to approximately 5 Hz.

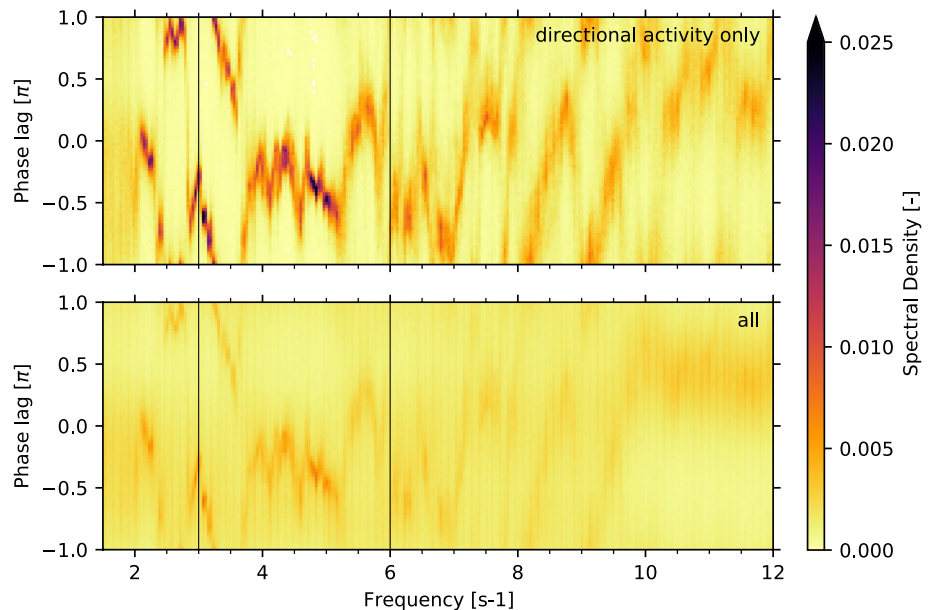


Figure 15. ZR phase lag spectral density for the signal-windowed cross-correlation functions (CCFs) of H03S1 with RAR in the vertical plane. (top) Eligible CCFs only (see Section 5) and (bottom) all CCFs of the 2014–2020 period. Vertical black lines indicate the filter frequencies and octave bands. Similar phase lags densities for H03S2 and H03S3 are given in Figures S3 and S4 in Supporting Information S1, respectively.

9. Discussions and Conclusion

This study demonstrates the retrieval of hydroacoustic travel time variations by time-lapse analysis of a triplet hydrophone station relative to a three-component broadband seismometer. Retrieved travel time variations are a proxy for path averaged changes in the deep-ocean temperature (Dushaw et al., 2009; Munk, 2006; W. Wu et al., 2020).

The proposed pre-processing workflow overcomes the differences in instrument sensitivity and sample rates, retaining phase and spectral information for the cross-correlation analysis. The obtained CCFs highly depend on the location of the seismometer. The latter requires a direct line of sight as well as adequate T-phase coupling. CCFs reveal the modal structure of the signal in agreement with an acoustic signal propagating through the SOFAR channel. The time-lapse analysis is applied to the band-limited spectrogram of the eligible CCF signal windows per receiver pair. The two discrete frequency bands, of 3–6 and 6–12 Hz, confine the two prominent modal peaks. The particular modal shape, with low frequencies arriving later, may be related to mode conversion near the receivers. Range dependent propagation modeling by, for example, Parabolic Equations, is recommended to understand the modal propagation and conversion. The peak of the two-dimensional cross-correlation coefficient of the spectrograms yields the variation in time lag and frequency and quantifies the change of the medium and the source. Variations in time lags correspond to frequency-dependent velocity changes, which are a proxy for deep-ocean thermometry. Frequency variations resemble a change in source signature—follow up research to further exploit these is recommended.

We assume that the MVC source is stationary. Any variation in source signature or location may affect the time-lapse analysis, resulting in a reduced 2D CCF and a frequency shift, lowering the weight and thus contribution for the mean lag time variation. Using additional hydroacoustic and seismic stations could quantify the variation in source location, which is recommended for further research.

The quality of the frequency-limited spectrogram is of utmost importance for the time-lapse analysis. Based on the STFT, the spectrogram has a uniform temporal and spectral resolution that depends only on the length of the Fourier transformed time window. This parameter, however, induces a time-frequency trade-off. A short time window confines the impulsive CCF signal but causes low spectral resolution and smearing, whereas a long time window improves the spectral resolution but is often too wide, including noise and spurious signals. A solution is to optimize spectrogram parameters per octave band using the multi-time-window FFT or the wavelet-based scaleogram over the spectrogram.

The scaling properties of the wavelet transform yield multiresolution temporal and spectral properties, supporting large time windows for low frequencies while maintaining short time windows for high frequencies. Still, the time-lapse analysis correlates energy and ignores any phase information between eligible CCFs. Time-lapse analysis, including phase information, can be obtained by frequency domain Fisher analysis using the phase-aligned cross-spectrum (e.g., Evers, 2008; Smart & Flinn, 2010). The Fisher analysis provides the Fisher coherence ratio and the corresponding theoretical noise-floor threshold. Furthermore, our method to extract the travel time variation disregards a substantial part of the time-lapse information. The trimmed weighted mean time lag variation ignores larger frequency offsets containing potential (source) information.

The medium-induced travel time change over time is assumed to be equivalent to the trimmed weighted mean variation in time lag obtained from the time-lapse, per octave band, and assuming no variation of the source signature. The estimated travel time variation reveals both a complex periodic variation as well as a robust linear trend. The linear travel time decrease is assumed to be associated with net temperature increase and is larger around the SOFAR channel (higher-frequency octave) compared to the deep ocean (lower-frequency octave; Dushaw et al., 2009; Munk, 2006). The estimated peak periodicity of the travel time variation yields 1.9 and 1.1 yr, for the lower- and higher-frequency octave, respectively. Estimating the exact warming is non-trivial due to the non-uniform source activity and short time period of this study from a climatological perspective. The decreasing trend may correspond to lower values of ocean circulation oscillations, almost entirely controlled by surface wind forcing and deep water tides (Wunsch & Ferrari, 2004). Long-period oscillations are mainly due to the El Niño-Southern Oscillation. Typically, an El Niño occurs every 2–10 yr and severely affects the thermocline (Open University, 2001). Interactions with the Antarctic Circumpolar Current mainly control the seasonal variability (L. Wu et al., 2011). The thermohaline circulation causes deep water masses to form at the Antarctic

Circumpolar and to overturn past Australia into the Pacific. Atmospheric disturbances and mesoscale ocean eddies cause shorter-period oscillations affecting the ocean circulation and, in particular, the South Pacific gyre.

The difference in trend between the octave bands agrees with the difference in the vertical sampling of the SOFAR channel. The high-frequency mode is confined around the SOFAR channel axis, sampling less the deep ocean. The strongest warming is found near the sea surface and decreases with depth (IPCC, 2014; Lumpkin et al., 2020). However, observations of deep-ocean heat content trends of depths below 2,000 m are scarce.

The difference in the travel time variations between the cross-correlations with the vertical and radial components contains valuable information for follow-up research. The estimated ZR phase lag density shows a mixture of near-zero and 90° phase lags, depending on frequency. The phase lag response indicates a mixture of dilatational body waves and rotational LQ waves. Land-based seismometers on steep-sloped islands are essential to obtain full global coverage for the hydroacoustic network of the IMS. Including the horizontal seismic component can be used to understand the T-phase acoustic-to-seismic conversion better. Utilizing the cross-correlations of the hydrophones with the vertical, radial, and transverse components could even enable site effect analyses such as H/V spectral ratio methods.

Although this study only considers H03S and RAR, the methodology can in principle be applied to any other triplet hydrophone array and a three-component seismometer given a known source. In the case of a non-stationary source like an ensemble of separate earthquakes, the relative source-receiver distance becomes dynamic and thus also the signal window. The presented time-lapse analysis is still possible, however, with increased complexity.

Appendix A: Numerical Summary Measures

A1. Location

Most robust and resistant measure of central tendency of x is the *median*, the 0.5th sample quantile ($q_{0.5}$) of x . A conventional measure, however, non-robust nor resistant for outliers, is the *sample mean*,

$$\bar{x} = \frac{1}{n} \sum_{i=1}^n x_i, \quad (\text{A1})$$

with n the number of samples of the data set x . The *weighted mean* of x with weights w is then defined as,

$$\bar{x}_w = \frac{1}{\sum_{i=1}^n w_i} \sum_{i=1}^n w_i x_i. \quad (\text{A2})$$

A more robust and resistant measure of central tendency including information of the magnitude of the data compared to the median is the *trimean*,

$$\text{Trimean}(x) = \frac{q_{0.25}(x) + 2q_{0.5}(x) + q_{0.75}(x)}{4}, \quad (\text{A3})$$

with q_p the p th sample quantile of x .

A2. Spread

The most robust and resistant measure of the spread or scale of a data set x is the *Interquartile Range* (IQR),

$$\text{IQR}(x) = q_{0.75}(x) - q_{0.25}(x). \quad (\text{A4})$$

The most conventional scale of a data set, however, is the *sample standard deviation*,

$$s(x) = \sqrt{\frac{1}{n-1} \sum_{i=1}^n (x_i - \bar{x})^2}, \quad (\text{A5})$$

with s^2 known as the *sample variance* of x . The standard deviation is non-robust nor resistant for outliers. The *weighted standard deviation* denotes

$$s_w(x) = \sqrt{\frac{n'}{(n' - 1)} \frac{1}{\sum_{i=1}^n w_i} \sum_{i=1}^n w_i (x_i - \bar{x}_w)^2}, \quad (\text{A6})$$

with n' the number of non-zero weights.

Appendix B: Unfiltered Time-Lapse Results

Figures B1 and B2 show the raw time-lapse results containing all time window combinations for the 3–6 Hz and 6–12 Hz octave bands, respectively.

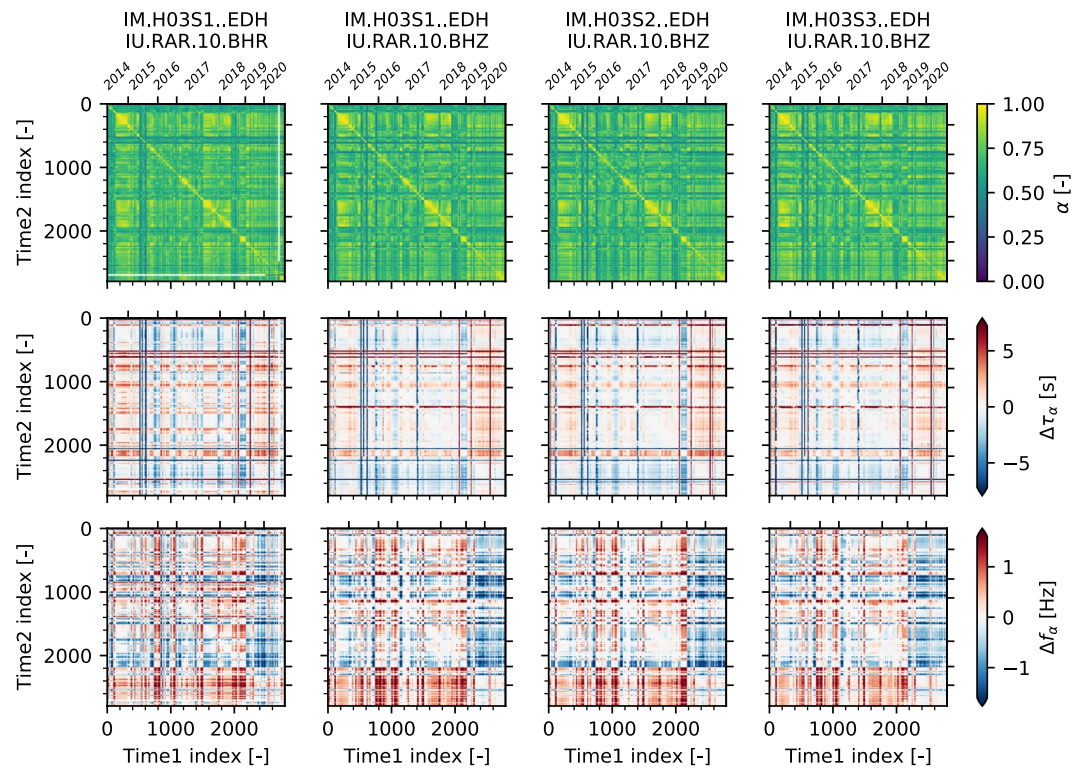


Figure B1. Time-lapse results for the 3–6 Hz octave band containing all time window combinations.

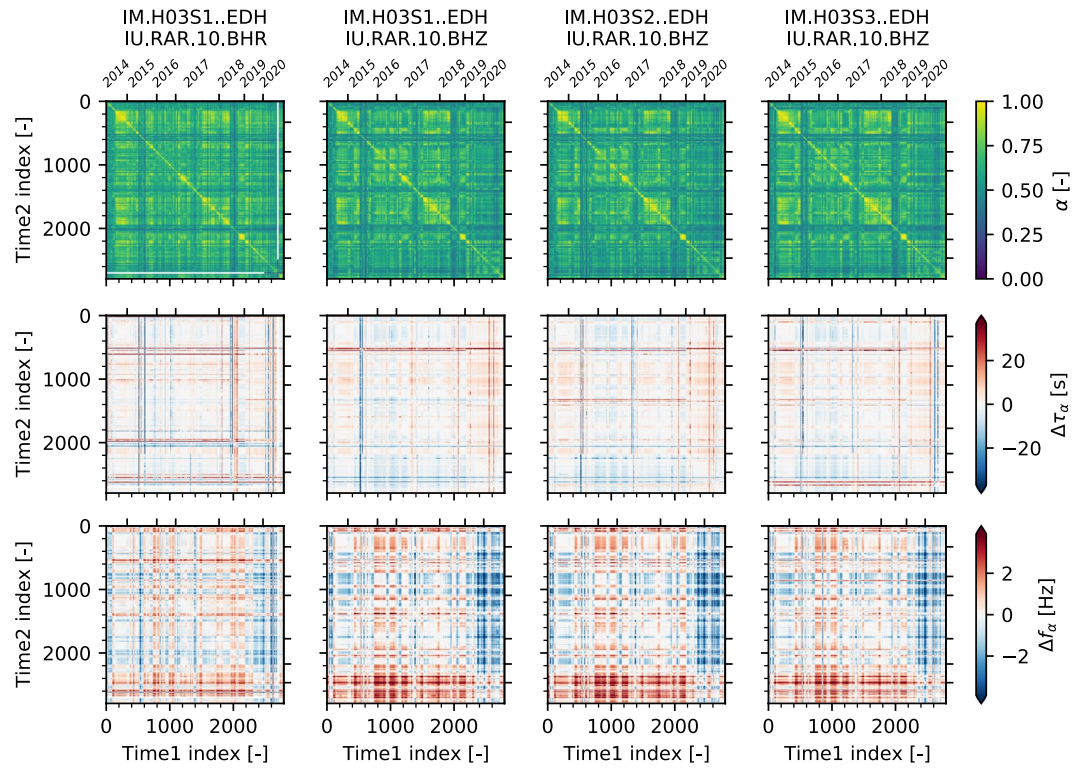


Figure B2. Time-lapse results for the 6–12 Hz octave band, containing all time window combinations.

Appendix C: Trimean Distributions of the Time-Lapse Parameters

Figures C1, C2 and C3 show the trimean distributions of the parameters α , Δf_α , and $\Delta \tau_\alpha$ of the raw time-lapse results shown in Figures B1 and B2. The trimean distributions are used to filter spurious time steps of the time-lapse analyses (see Section 6).

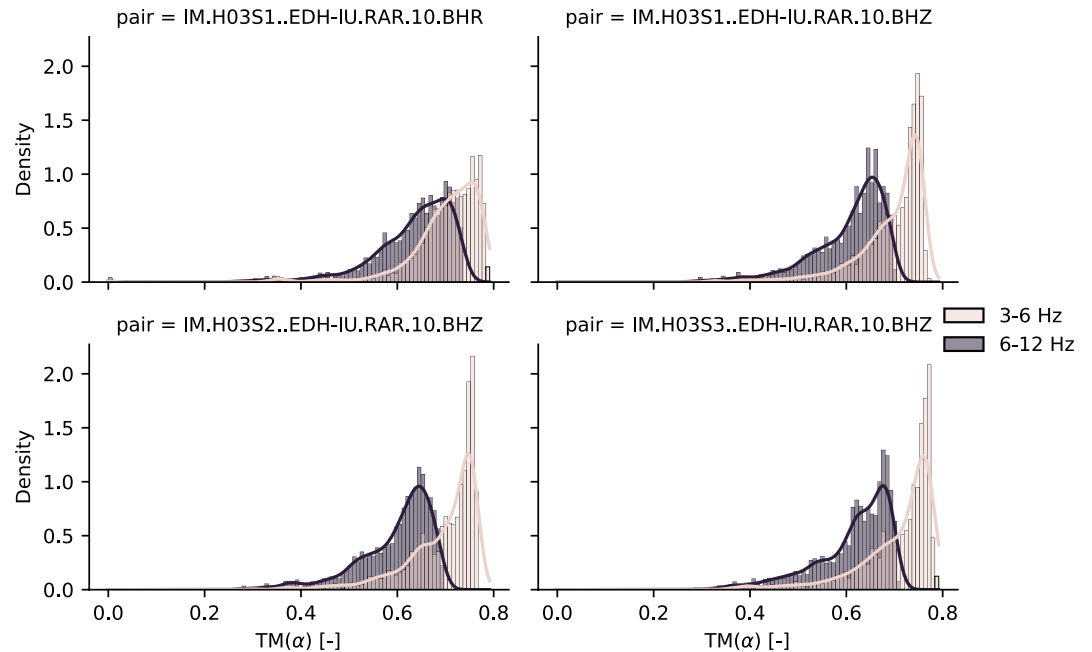


Figure C1. Trimean distribution for the unfiltered time-lapse peak 2D CCF (α) per time step.

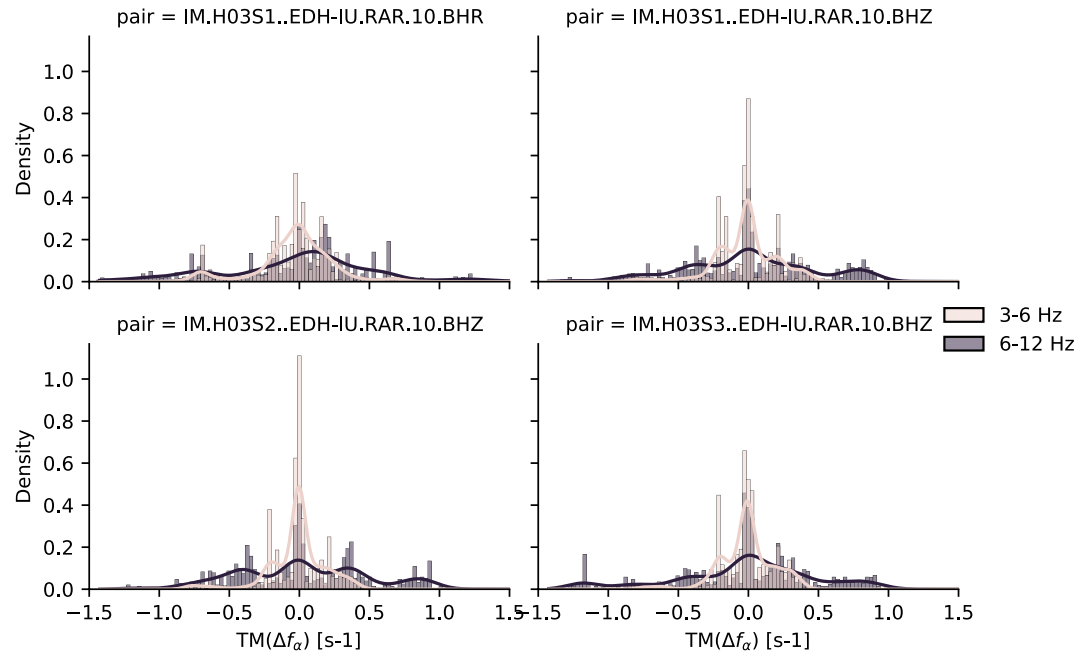


Figure C2. Trimean distribution for the unfiltered time-lapse frequency lag Δf_α per time step.

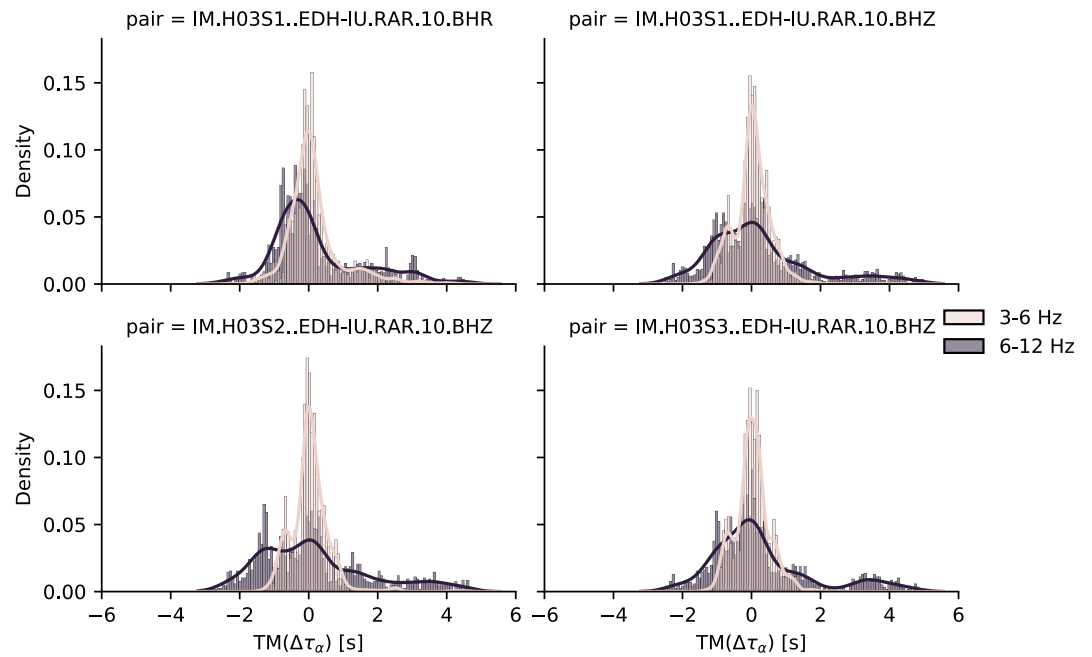


Figure C3. Trimean distribution for the filtered time-lapse time lag $\Delta \tau_\alpha$ per time step.

Data Availability Statement

Hydroacoustic data can be requested at the CTBTO International DataCenter (IDC) in Vienna, via the virtual Data Exploration Center. Broadband seismic data and hydroacoustic data of H10 since 2015 are openly available on IRIS (<https://iris.edu>). Data sets of all results except the CCFs are available on the data repository 4TU.ResearchData with DOI <https://doi.org/10.4121/19063838>. CCFs are available upon request (~1.5 TB). The source code is available on GitHub (<https://github.com/psmsmets/xcorr>) with DOI <https://doi.org/10.5281/zenodo.5883341> containing the Python3 module and examples. The code is build around ObsPy (<https://obspy.org>), NumPy (<https://numpy.org>), SciPy (<https://scipy.org>), xarray (<http://xarray.pydata.org>), pandas (<http://pandas.pydata.org>) and Dask (<https://dask.org>). Jupyter notebooks to reproduce all figures are available on GitHub (<https://github.com/psmsmets/xcorr-cookbook-data>) with DOI [10.5281/zenodo.5902705](https://doi.org/10.5281/zenodo.5902705). Figures were prepared using the Generic Mapping Tools (Wessel et al., 2019), Matplotlib (<https://matplotlib.org>), and Seaborn (<http://seaborn.pydata.org>).

Acknowledgments

The CTBTO station operators are thanked for the high-quality data and products. P.S. and L.E.'s contributions are funded through a VIDJ project from the Netherlands Organisation for Scientific Research (NWO), Grant No. 864.14.005. We thank two anonymous reviewers for their valuable feedback and comments.

References

- Bendat, J. S., & Piersol, A. G. (1987). *Random data: Analysis and measurement procedures* (4th ed.). Wiley. <https://doi.org/10.2307/2289430>
- Beyreuther, M., Barsch, R., Krischer, L., Megies, T., Behr, Y., & Wassermann, J. (2010). ObsPy: A Python toolbox for seismology. *Seismological Research Letters*, 81, 530–533. <https://doi.org/10.1785/gssrl.81.3.530>
- Bishop, J. W., Fee, D., & Szuberla, C. A. L. (2020). Improved infrasound array processing with robust estimators. *Geophysical Journal International*, 221, 2058–2074. <https://doi.org/10.1093/gji/ggaa110>
- Dahlman, O., Mykkeltveit, S., & Haak, H. (2009a). Monitoring technologies. In *Nuclear test ban* (pp. 25–58). Springer Netherlands. https://doi.org/10.1007/978-1-4020-6885-0_2
- Dahlman, O., Mykkeltveit, S., & Haak, H. (2009b). The treaty. In *Nuclear test ban* (pp. 83–98). Springer Netherlands. https://doi.org/10.1007/978-1-4020-6885-0_4
- Davey, F. J. (1980). The Monowai seamount: An active submarine volcanic centre on the Tonga-Kermadec ridge (note). *New Zealand Journal of Geology and Geophysics*, 23(4), 533–536. <https://doi.org/10.1080/00288306.1980.10424124>
- de Groot-Hedlin, C. D. (2005). Estimation of the rupture length and velocity of the Great Sumatra earthquake of 26 December 2004 using hydroacoustic signals. *Geophysical Research Letters*, 32(11). <https://doi.org/10.1029/2005GL022695>
- De Groot-Hedlin, C. D., & Orcutt, J. (2000). *Detection of T-phases at island seismic stations: Dependence on seafloor slope, seismic velocity and roughness (Tech. Rep.)*. University of California, Scripps Institution of Oceanography.
- Dushaw, B. D., Worcester, P. F., Munk, W. H., Spindel, R. C., Mercer, J. A., Howe, B. M., et al. (2009). A decade of acoustic thermometry in the North Pacific Ocean. *Journal of Geophysical Research: Oceans*, 114, C07021. <https://doi.org/10.1029/2008JC005124>
- Edwards, W. N., & Green, D. N. (2012). Effect of interarray elevation differences on infrasound beamforming. *Geophysical Journal International*, 190(1), 335–346. <https://doi.org/10.1111/j.1365-246X.2012.05465.x>
- Evers, L. G. (2008). *The inaudible symphony: On the detection and source identification of atmospheric infrasound, (Unpublished doctoral dissertation)*. Delft University of Technology.
- Evers, L. G., Green, D. N., Young, N. W., & Snellen, M. (2013). Remote hydroacoustic sensing of large icebergs in the southern Indian Ocean: Implications for iceberg monitoring. *Geophysical Research Letters*, 40, 4694–4699. <https://doi.org/10.1002/grl.50914>
- Evers, L. G., & Snellen, M. (2015). Passive probing of the sound fixing and ranging channel with hydro-acoustic observations from ridge earthquakes. *Journal of the Acoustical Society of America*, 137, 2124–2136. <https://doi.org/10.1121/1.4916267>
- Evers, L. G., Wapenaar, K., Heaney, K. D., & Snellen, M. (2017). Deep ocean sound speed characteristics passively derived from the ambient acoustic noise field. *Geophysical Journal International*, 210, 27–33. <https://doi.org/10.1093/gji/ggx061>
- Fowler, C. M. (2005). *The solid Earth: An introduction to global geophysics* (2nd ed.). Cambridge University Press. <https://doi.org/10.1029/90eo00309>
- Green, D. N., Evers, L. G., Fee, D., Matoza, R. S., Snellen, M., Smets, P., & Simons, D. (2013). Hydroacoustic, infrasonic, and seismic monitoring of the submarine eruptive activity and sub-aerial plume generation at South Sarigan, May 2010. *Journal of Volcanology and Geothermal Research*, 257, 31–43. <https://doi.org/10.1016/j.jvolgeores.2013.03.006>
- Groos, J. C. (2010). *Broadband seismic noise: Classification and Green's function estimation, (dissertation)*. Karlsruher Institut für Technologie. <https://doi.org/10.13140/2.1.3658.4489>
- Haralabus, G., Pautet, L., Stanley, J., & Zampolli, M. (2014). Welcome back HA03 Robinson Crusoe Island. *CTBTO Spectrum*, 22, 18–22.
- IPCC. (2014). Observations: Ocean pages. In *Climate change 2013—The physical science basis: Working Group I Contribution to the Fifth Assessment Report of the Intergovernmental Panel on Climate Change* (pp. 255–316). Cambridge University Press. <https://doi.org/10.1017/CBO9781107415324.010>
- Jensen, F. B., Kuperman, W. A., Porter, M. B., & Schmidt, H. (2011). *Computational ocean acoustics* (2nd ed.). Springer. <https://doi.org/10.1007/978-1-4419-8678-8>
- Kästle, E. D., Soomro, R., Weemstra, C., Boschi, L., & Meier, T. (2016). Two-receiver measurements of phase velocity: Cross-validation of ambient-noise and earthquake-based observations. *Geophysical Journal International*, 207, 1493–1512. <https://doi.org/10.1093/gji/ggw341>
- Kuna, V. M., & Nábělek, J. L. (2021). Seismic crustal imaging using fin whale songs. *Science*, 371(6530), 731–735. <https://doi.org/10.1126/science.abf3962>
- Locarnini, R. A., Mishonov, A. V., Antonov, J. I., Boyer, T. P., Garcia, H. E., Baranova, O. K., & Seidov, D. (2013). *World Ocean Atlas 2013 volume 1: Temperature*. In S. Levitus & A. Mishonov (Eds.), (Vol. 73). NOAA Atlas NESDIS.
- Lumpkin, R., Baringer, M., Bif, M. B., Boyer, T., Bushinsky, S. M., Carter, B. R., et al. (2020). Global oceans. *Bulletin of the American Meteorological Society*, 101(8), S129–S184. <https://doi.org/10.1175/BAMS-D-20-0105.1>
- Matsumoto, H., Bohnenstiehl, D. R., Tournadre, J., Dziak, R. P., Haxel, J. H., Lau, T.-K. A., et al. (2014). Antarctic icebergs: A significant natural ocean sound source in the Southern Hemisphere. *Geochemistry, Geophysics, Geosystems*, 15(8), 3448–3458. <https://doi.org/10.1002/2014GC005454>

- Metz, D., Watts, A. B., Grevemeyer, I., & Rodgers, M. (2018). Tracking submarine volcanic activity at Monowai: Constraints from long-range hydroacoustic measurements. *Journal of Geophysical Research: Solid Earth*, *123*, 7877–7895. <https://doi.org/10.1029/2018JB015888>
- Metz, D., Watts, A. B., Grevemeyer, I., Rodgers, M., & Paulatto, M. (2016). Ultra-long-range hydroacoustic observations of submarine volcanic activity at Monowai, Kermadec Arc. *Geophysical Research Letters*, *43*, 1529–1536. <https://doi.org/10.1002/2015GL067259>
- MSFD. (2008). *DIRECTIVE 2008/56/EC OF THE EUROPEAN PARLIAMENT AND OF THE COUNCIL of 17 June 2008: establishing a framework for community action in the field of marine environmental policy (Marine Strategy Framework Directive)*. Official Journal of the European Union.
- Munk, W. (2006). Ocean acoustic tomography from a stormy start to an uncertain future. In *Physical oceanography: developments since 1950* (pp. 119–138). Springer New York. https://doi.org/10.1007/0-387-33152-2_8
- Nichols, S. M., & Bradley, D. L. (2017). In situ shape estimation of triangular moored hydrophone arrays using ambient signals. *IEEE Journal of Oceanic Engineering*, *42*, 923–935. <https://doi.org/10.1109/OJOE.2016.2625378>
- Open University (2001). *Ocean circulation* (2nd ed.). Butterworth Heinemann.
- Pedregosa, F., Varoquaux, G., Gramfort, A., Michel, V., Thirion, B., Grisel, O., & Duchesnay, É. (2011). Scikit-learn: Machine learning in Python. *Journal of Machine Learning Research*, *12*, 2825–2830.
- Prior, M., Brown, D., Haralabus, G., Stanley, J., & Institute of Acoustics (Great Britain). (2012). *Long-term monitoring of ambient noise at CTBTO hydrophone stations*. In (pp. 1018–1025). Institute Of Acoustics.
- Roux, P., & Kuperman, W. A. (2004). Extracting coherent wavefronts from acoustic ambient noise in the ocean. *Journal of the Acoustical Society of America*, *116*, 1995–2003. <https://doi.org/10.1121/1.1797754>
- Sambell, K. A. M., Smets, P. S. M., Simons, D. G., Snellen, M., & Evers, L. G. (2019). A study on the ambient noise field at a hydroacoustic array near Robinson Crusoe Island. *Geophysical Journal International*, *218*, 88–99. <https://doi.org/10.1093/gji/ggz124>
- Smart, E., & Flinn, E. A. (2010). Fast frequency-wavenumber analysis and fisher signal detection in real-time infrasonic array data processing. *Geophysical Journal of the Royal Astronomical Society*, *26*(1–4), 279–284. <https://doi.org/10.1111/j.1365-246X.1971.tb03401.x>
- Snieder, R. (2004). Extracting the Green's function from the correlation of coda waves: A derivation based on stationary phase. *Physical Review E—Statistical Physics, Plasmas, Fluids, and Related Interdisciplinary Topics*, *69*, 8. <https://doi.org/10.1103/PhysRevE.69.046610>
- Szuberla, C. A. L., & Olson, J. V. (2004). Uncertainties associated with parameter estimation in atmospheric infrasound arrays. *Journal of the Acoustical Society of America*, *115*, 253–258. <https://doi.org/10.1121/1.1635407>
- Takagi, R., Nishida, K., Aoki, Y., Maeda, T., Masuda, K., Takeo, M., et al. (2015). A single bit matters: Coherent noise of seismic data loggers. *Seismological Research Letters*, *86*(3), 901–907. <https://doi.org/10.1785/0220150030>
- Talandier, J., Hyvernaud, O., Reymond, D., & Okal, E. A. (2006). Hydroacoustic signals generated by parked and drifting icebergs in the Southern Indian and Pacific Oceans. *Geophysical Journal International*, *165*(3), 817–834. <https://doi.org/10.1111/j.1365-246X.2006.02911.x>
- Tanimoto, T., & Rivera, L. (2005). Prograde Rayleigh wave particle motion. *Geophysical Journal International*, *162*, 399–405. <https://doi.org/10.1111/j.1365-246X.2005.02481.x>
- Wapenaar, K., Draganov, D., Snieder, R., Campman, X., & Verdel, A. (2010). Tutorial on seismic interferometry: Part 1 —Basic principles and applications. *Geophysics*, *75*, 75A195–75A209. <https://doi.org/10.1190/1.3457445>
- Wapenaar, K., Fokkema, J., & Snieder, R. (2005). Retrieving the Green's function in an open system by cross-correlation: A comparison of approaches (L). *Journal of the Acoustical Society of America*, *118*, 2783–2786. <https://doi.org/10.1121/1.2046847>
- Watts, A. B., Peirce, C., Grevemeyer, I., Paulatto, M., Stratford, W., Bassett, D., et al. (2012). Rapid rates of growth and collapse of Monowai submarine volcano in the Kermadec Arc. *Nature Publishing Group*, *5*(7), 510–515. <https://doi.org/10.1038/ngeo1473>
- Weaver, R. L., & Lobkis, O. I. (2001). Ultrasonics without a source: Thermal fluctuation correlations at MHz frequencies. *Physical Review Letters*, *87*, 134301. <https://doi.org/10.1103/PhysRevLett.87.134301>
- Weemstra, C., de Laat, J. I., Verdel, A., & Smets, P. (2020). Systematic recovery of instrumental timing and phase errors using interferometric surface waves retrieved from large-N seismic arrays. *Geophysical Journal International*, *224*, 1028–1055. <https://doi.org/10.1093/gji/ggaa504>
- Wessel, P., Luis, J. F., Uieda, L., Scharroo, R., Wobbe, F., Smith, W. H., & Tian, D. (2019). The generic mapping tools version 6. *Geochemistry, Geophysics, Geosystems*, *20*, 5556–5564. <https://doi.org/10.1029/2019GC008515>
- Wilkinson, M. D., Dumontier, M., Aalbersberg, I. J., Appleton, G., Axton, M., Baak, A., et al. (2016). The FAIR guiding principles for scientific data management and stewardship. *Scientific Data*, *3*, 160018. <https://doi.org/10.1038/sdata.2016.18>
- Woolfe, K. F., Lani, S., Sabra, K. G., & Kuperman, W. A. (2015). Monitoring deep-ocean temperatures using acoustic ambient noise. *Geophysical Research Letters*, *42*, 2878–2884. <https://doi.org/10.1002/2015GL063438>
- Woolfe, K. F., & Sabra, K. G. (2015). Variability of the coherent arrivals extracted from low-frequency deep-ocean ambient noise correlations. *Journal of the Acoustical Society of America*, *138*(2), 521–532. <https://doi.org/10.1121/1.4923447>
- Wu, L., Jing, Z., Riser, S., & Visbeck, M. (2011). Seasonal and spatial variations of Southern Ocean diapycnal mixing from Argo profiling floats. *Nature Geoscience*, *4*(6), 363–366. <https://doi.org/10.1038/ngeo1156>
- Wu, W., Zhan, Z., Peng, S., Ni, S., & Callies, J. (2020). Seismic ocean thermometry. *Science*, *369*, 1510–1515. <https://doi.org/10.1126/science.abb9519>
- Wunsch, C., & Ferrari, R. (2004). Vertical mixing, energy, and the general circulation of the oceans. *Annual Review of Fluid Mechanics*, *36*(1), 281–314. <https://doi.org/10.1146/annurev.fluid.36.050802.122121>
- Yildiz, S., Sabra, K., Dorman, L. M., & Kuperman, W. A. (2013). Using hydroacoustic stations as water column seismometers. *Geophysical Research Letters*, *40*(11), 2573–2578. <https://doi.org/10.1002/grl.50371>
- Zweng, M. M., Reagan, J. R., Antonov, I., Locarnini, R. A., Mishonov, A. V., Boyer, T. P., et al. (2013). *World Ocean Atlas 2013, volume 2: Salinity*. In S. Levitus & A. Mishonov (Eds.), (Vol. 74). NOAA Atlas NESDIS.